

Collective response and noise of a levitated ferromagnet lattice for ultralight dark matter detection

Dongyi Yang,¹ Xiao Yang,² Chenxi Sun,^{2,*} and Jianwei Zhang^{1,†}

¹*School of Physics, Peking University, Beijing 100871, China*

²*Beijing Key Laboratory of Quantum Sensing and Precision Measurement,*

and Center for Quantum Information Technology,

and Institute of Quantum Electronics,

Peking University, Beijing 100871, China

(Dated: May 19, 2026)

arXiv:2605.17417v1 [hep-ph] 17 May 2026

Abstract

Ultralight dark matter can induce weak oscillating magnetic-like signals and can therefore be searched for with precision magnetometry. Levitated ferromagnets provide a sensitive platform for such searches, but a single ferromagnet is limited in total polarized spin and readout performance. We investigate a levitated ferromagnet lattice as a scalable detector for ultralight dark matter. We develop a theoretical description of the collective lattice response in the fully trapped regime, incorporating dipole-dipole interactions, finite-size effects, and boundary-induced mode mixing. We further analyze the collective noise budget and show that interaction effects mainly produce a narrow blind zone through thermal-noise amplification, while away from this region, the lattice preserves favorable collective noise scaling. We then derive projected sensitivities to axion-electron, dark-photon, and axion-photon couplings. We find that the lattice improves the reach in all three channels relative to a single-ferromagnet detector, with an additional coherent signal enhancement in the axion-photon channel from the lattice-generated electromagnetic background.

I. INTRODUCTION

Ultralight dark matter (ULDM) candidates, including axions, axion-like particles, and dark photons, can be described as classical, coherently oscillating fields on laboratory scales [1–3]. Their oscillation frequencies are set by their masses, typically spanning a wide range from sub-Hz to kHz and beyond. In this regime, ULDM interacts with standard-model particles through effective couplings that can be interpreted as oscillating, spatially coherent forces or fields, providing a promising target for precision measurement experiments [4–6].

A number of experimental approaches have been proposed and implemented to probe such signals, including nuclear magnetic resonance, atomic magnetometry, torsion balances, and resonant electromagnetic detectors [7–9]. Among these, levitated ferromagnets have recently emerged as a sensitive platform for detecting spin-dependent interactions of ULDM [10]. In these systems, the intrinsic spin of a ferromagnet couples to external magnetic-like fields induced by dark matter, and the resulting mechanical motion can be read out with high precision. The sensitivity of such detectors is determined by the interplay between the

* scx@pku.edu.cn

† james@pku.edu.cn

intrinsic susceptibility of the ferromagnet and the noise properties of the readout system.

A natural direction for improving the sensitivity of such detectors is to extend from a single ferromagnet to an array of many identical elements. The basic idea and its leading-order sensitivity gain were introduced in our recent letter [11]. In this work, we investigate a ferromagnet lattice as a platform for ULDM detection. The key idea is to perform a collective readout of a large number of ferromagnets, thereby enhancing the effective signal-to-noise ratio while preserving the intrinsic dynamics of each individual element. Unlike simply increasing the size of a single magnet, this approach allows one to scale up the total polarized spin without significantly altering the single-particle response, providing a route to improved sensitivity that is compatible with existing levitation and readout techniques.

The transition from a single particle to a lattice, however, introduces several new physical ingredients that must be treated carefully. First, dipole-dipole interactions between ferromagnets modify the dynamical response of the system, leading to a momentum-dependent susceptibility and the emergence of collective modes. Second, the finite size of the lattice breaks translational invariance, resulting in boundary-induced mode mixing that couples the coherent ($k = 0$) mode to other modes. Third, the noise properties of the detector are altered in a nontrivial way: different noise sources scale differently with the number of particles, and interaction-induced mode mixing can significantly modify the effective noise spectrum. A consistent treatment of these effects is necessary in order to reliably assess the performance of the lattice detector.

In this paper, we develop a theoretical framework that incorporates these ingredients in a unified manner. We first describe the single-particle dynamics in terms of a susceptibility matrix in the fully trapped regime. We then generalize this description to a periodic lattice, introducing the interaction kernel in momentum space and identifying the coherent mode that couples to spatially uniform signals. The effects of finite size are captured by a boundary-induced self-energy, which modifies the response of the coherent channel and gives rise to characteristic features such as near-singular modes and blind zones. Building on this dynamical description, we analyze the noise properties of the lattice, including thermal, imprecision, and backaction contributions, and determine how they combine to set the final sensitivity.

Using this framework, we evaluate the projected sensitivities of the ferromagnet lattice for three representative ULDM couplings: axion-electron, dark-photon, and axion-photon

interactions. We find that the lattice configuration improves the reach in all three cases compared to a single-ferromagnet detector, primarily through the collective reduction of the effective noise floor. In the axion-photon channel, the signal also receives an additional coherent enhancement associated with the electromagnetic response of the lattice, leading to a more pronounced improvement with increasing particle number. Overall, the lattice provides a systematic and scalable way to enhance sensitivity across multiple ULDM scenarios.

The remainder of this paper is organized as follows. In Sec. II, we review the dynamics of a single levitated ferromagnet and introduce the susceptibility formalism. In Sec. III, we describe the lattice configuration and relevant experimental considerations. In Sec. IV, we develop the theoretical framework for the lattice response, including interaction effects and boundary-induced mode mixing. In Sec. V, we analyze the noise properties of the lattice detector. In Sec. VI, we apply the framework to ULDM detection and present projected sensitivities. Finally, we summarize our results and discuss future directions in Sec. VII.

II. SINGLE LEVITATED FERROMAGNET

We consider a single levitated ferromagnetic particle with a large, macroscopically polarized spin. The internal magnetization is assumed to be rigidly locked to the body of the particle, such that the spin degrees of freedom can be described by a single unit vector

$$\hat{\mathbf{n}} = \frac{\mathbf{S}}{|\mathbf{S}|}, \quad (1)$$

where \mathbf{S} denotes the total spin angular momentum of the ferromagnet. The magnetic moment of the ferromagnet is given by

$$\boldsymbol{\mu} = -\gamma_e \mathbf{S} = \mu \hat{\mathbf{n}}, \quad (2)$$

where γ_e is the electron gyromagnetic ratio, and $\mu = -\gamma_e |\mathbf{S}|$. In addition to its intrinsic spin, the particle possesses mechanical angular momentum \mathbf{L} , associated with rigid-body rotation. The total angular momentum is therefore

$$\mathbf{J} = \mathbf{L} + \mathbf{S}. \quad (3)$$

The ferromagnet is assumed to be levitated in a trapping potential that fixes its center-of-mass position. Throughout this work, we focus on the rotational dynamics and neglect

translational degrees of freedom. The orientation of the ferromagnet is fully specified by the direction of $\hat{\mathbf{n}}$, which we parametrize using spherical angles (θ, ϕ) with respect to a fixed laboratory frame. The particle is subject to an orientation-dependent potential $V(\hat{\mathbf{n}})$, which denotes the total potential energy relevant to the rotational dynamics. It may include contributions from the trapping potential, residual magnetic fields, gravity-induced torques, or other externally engineered fields. This potential defines one or more equilibrium orientations of the magnetization. In addition, weak time-dependent magnetic fields may act on the spin degree of freedom and serve either as probe signals or as external drives. Dissipation is assumed to be negligible on the timescales of interest, consistent with the high mechanical quality factors achievable in levitated systems.

The equations of motion of the ferromagnet can be written as

$$\partial_t \mathbf{J} = -\hat{\mathbf{n}} \times \nabla_{\hat{\mathbf{n}}} V, \quad \partial_t \hat{\mathbf{n}} = \boldsymbol{\Omega} \times \hat{\mathbf{n}}, \quad (4)$$

where $\boldsymbol{\Omega}$ is the angular velocity of the rigid body and the mechanical angular momentum satisfies $\mathbf{L} = I\boldsymbol{\Omega}$, with I the moment of inertia of the ferromagnet. In the following, we assume that the ferromagnets are spherically symmetric, so that I is a scalar. In that case, one can show that

$$j_n \equiv \frac{\mathbf{J} \cdot \hat{\mathbf{n}}}{S} \quad (5)$$

is a constant of motion. Physically, j_n characterizes the projection of the total angular momentum onto the magnetization direction. In the generic situations considered in this work, it is an $\mathcal{O}(1)$ dynamical invariant and is typically taken to be $j_n = 1$. For the equilibrium configuration around which we linearize, we separate the weak time-dependent probe field from the static orientational potential. The equilibrium orientation $\hat{\mathbf{n}}_0$ is therefore determined by the static trapping part of the potential,

$$\nabla_{\hat{\mathbf{n}}} V_{\text{trap}} \Big|_{\hat{\mathbf{n}}_0} = 0. \quad (6)$$

We study the response of the system to weak perturbations about this equilibrium. Writing $\theta(t) = \theta_0 + \delta\theta(t)$ and $\phi(t) = \phi_0 + \delta\phi(t)$, and assuming small angular deviations, the equations of motion can be linearized in $\delta\theta$ and $\delta\phi$.

To leading order, the dynamics are fully captured by a set of coupled linear equations for

the angular fluctuations, reading [10]

$$\left[\partial_t^2 \begin{pmatrix} 1 & 0 \\ 0 & \sin^2 \theta_0 \end{pmatrix} + j_n \omega_I \sin \theta_0 \partial_t \begin{pmatrix} 0 & 1 \\ -1 & 0 \end{pmatrix} + \omega_I \begin{pmatrix} v_{\theta\theta} & v_{\theta\phi} \\ v_{\phi\theta} & v_{\phi\phi} \end{pmatrix} \right] \begin{pmatrix} \delta\theta \\ \delta\phi \end{pmatrix} = 0, \quad (7)$$

where

$$\omega_I = \frac{|\mu|}{\gamma_e I} \quad (8)$$

is the Einstein-de Haas frequency, and

$$v_{ij} = \left. \frac{\gamma_e}{|\mu|} \frac{\partial^2 V_{\text{trap}}}{\partial i \partial j} \right|_{\hat{\mathbf{n}}_0}, \quad i, j \in \{\theta, \phi\}, \quad (9)$$

encode the local curvature of the trapping potential at equilibrium. External time-dependent magnetic fields enter as driving terms through their coupling to the magnetic moment. In the frequency domain, the linearized equations define a susceptibility matrix that relates the angular response of the ferromagnet to an applied oscillatory magnetic field.

Rather than reproducing the full derivation, which has been presented in detail in ref. [10], we summarize the resulting linear response in terms of the susceptibility matrix. For a weak oscillating magnetic field $\mathbf{B}(t) = \mathbf{B}_0 e^{-i\omega t}$, the angular response of the ferromagnet takes the form

$$\begin{pmatrix} \delta\theta(\omega) \\ \delta\phi(\omega) \end{pmatrix} = -\mu B_0 \chi(\omega) \begin{pmatrix} b_\theta \\ b_\phi \end{pmatrix}, \quad (10)$$

where (b_θ, b_ϕ) denote the components of the magnetic field in the local angular basis. The inverse susceptibility matrix is given by

$$\chi(\omega)^{-1} = I \left[-\omega^2 \begin{pmatrix} 1 & 0 \\ 0 & 1 \end{pmatrix} - i j_n \omega_I \omega \begin{pmatrix} 0 & 1 \\ -1 & 0 \end{pmatrix} + \omega_I \begin{pmatrix} v_{\theta\theta} & 0 \\ 0 & v_{\phi\phi} \end{pmatrix} \right], \quad (11)$$

where we choose local coordinates such that the equilibrium orientation is represented by $\theta_0 = \pi/2$ and $\phi_0 = 0$. We further diagonalize the curvature matrix at the equilibrium point, so that

$$v_{ij} = \text{diag}(v_{\theta\theta}, v_{\phi\phi}), \quad v_{\theta\theta} > 0, \quad v_{\phi\phi} > 0. \quad (12)$$

Equation (11) is the general linearized susceptibility matrix near the equilibrium orientation. It contains both oscillatory and precessional responses: the diagonal terms encode trap-induced libration, while the antisymmetric term proportional to $j_n \omega_I \omega$ describes precessional mixing associated with angular-momentum conservation. Different limits of Eq. (11)

correspond to distinct dynamical regimes, including fully trapped, partially trapped, and gyroscopic motion. In the present work, however, our main focus is the fully trapped regime, in which the orientational dynamics are dominated by the restoring torques of the trap.

In the fully trapped regime, the trapping potential provides restoring torques in both angular directions transverse to the equilibrium orientation. This is the primary operating regime considered in this work. Although the general susceptibility in Eq. (11) contains a precessional mixing term proportional to $j_n \omega_1 \omega$, the response in the parameter range of interest is dominated by trap-induced libration. Accordingly, in the following analysis we adopt the oscillation-dominated approximation and use the simplified inverse susceptibility

$$\chi^{-1}(\omega) = I \begin{pmatrix} -\omega^2 + \omega_1 v_{\theta\theta} & 0 \\ 0 & -\omega^2 + \omega_1 v_{\phi\phi} \end{pmatrix}. \quad (13)$$

The two eigenfrequencies are therefore

$$\omega_{\theta,\phi} = \sqrt{\omega_1 v_{\theta\theta,\phi\phi}}. \quad (14)$$

These two modes correspond to small-angle librations about the equilibrium orientation. For frequencies well below resonance the response is quasi-static and set mainly by the trap stiffness. Very close to resonance, the susceptibility is enhanced and the neglected precessional mixing can modify the detailed lineshape. At frequencies above the larger libration frequency, the response is rapidly suppressed, so that the largest resonance frequency also roughly defines the upper frequency limit of the efficient frequency band. The system can be optimized for maximal sensitivity in a narrow frequency range around a target resonance. In the present work, however, our primary interest is broadband sensitivity away from resonance. This fully trapped, oscillation-dominated regime provides the controlled starting point for the lattice analysis in the following sections.

In realistic experimental implementations, the trapping potential of a levitated ferromagnet generally includes contributions from residual magnetic fields inside the magnetic shielding. Even in multi-layer μ -metal shields, leakage fields at the level of $B_{\text{leak}} \sim 10^{-9}$ – 10^{-8} T are common. Such residual fields generate an orientational potential of the form

$$V(\hat{\mathbf{n}}) \simeq -\boldsymbol{\mu} \cdot \mathbf{B}_{\text{leak}}, \quad (15)$$

which produces a restoring torque for small angular deviations about the alignment direction. Expanding this potential to quadratic order around the alignment direction gives a trap

curvature of order $|\mu|B_{\text{leak}}$, which implies the parametric estimate

$$\omega_{\text{trap}}^2 \sim \frac{|\mu|B_{\text{leak}}}{I}. \quad (16)$$

For typical parameters of levitated micron-scale ferromagnets, even nanotesla-level leakage fields yield trapping frequencies well above the characteristic rotational frequency ω_I . As a result, complete rotational freedom is generally difficult to realize in present-day experiments, and the fully trapped regime is typically the most natural and experimentally relevant dynamical configuration.

For completeness, Eq. (11) also covers partially trapped and gyroscopic limits. In the partially trapped case, only one angular direction has finite restoring curvature, leading to a hybrid response with one librational and one nearly free rotational mode. In the gyroscopic limit, the restoring curvature vanishes in both directions and the dynamics are governed mainly by angular-momentum conservation. Since neither limit is central to the lattice design studied here, we do not discuss them further in detail. The partially trapped regime may nevertheless arise in situations where the residual field is effectively uniaxial and provides curvature only along one angular direction, for example in the presence of approximate axial symmetry. The gyroscopic regime requires that the orientational curvature be suppressed in both angular directions, which could occur in exceptionally well-shielded environments, in actively compensated field configurations, or outside the influence of the geomagnetic field in space. While such conditions are challenging and are not the primary focus of current implementations, they are not excluded in principle. The gyroscopic limit is therefore of conceptual interest and may be relevant for alternative measurement strategies that exploit long coherence times and slow precession rather than harmonic resonance.

III. FERROMAGNET LATTICE: GEOMETRY AND LEVITATION

A. Lattice geometry

We consider a lattice composed of N identical levitated ferromagnets, each of radius R , mass density ρ , magnetization M , and magnetic moment $\boldsymbol{\mu}_i$, where $\hat{\mathbf{n}}_i$ denotes the orientation of the intrinsic spin of the i th ferromagnet. The ferromagnets are positioned at fixed equilibrium locations \mathbf{r}_i , forming a three-dimensional crystal-like array with lattice constant

a_0 . The overall linear size of the lattice is $L_{\text{lat}} \sim N^{1/3}a_0$, and the lattice is enclosed within a magnetic shield of characteristic size L_{sh} . Throughout this work we assume the hierarchy

$$R \ll a_0 \ll L_{\text{lat}} \ll L_{\text{sh}}, \quad (17)$$

which ensures that (i) each ferromagnet behaves as a point magnetic dipole at inter-particle distances, (ii) the lattice occupies a region small compared with the shield size, and (iii) cavity modes of the shield vary slowly across the lattice volume. We also assume that each ferromagnet is sufficiently far from the shield, so that the direct influence of the shield on the lattice dynamics can be neglected. The influence of the approximation of this hierarchy will be discussed in section V.C.

Each ferromagnet retains its own rotational degrees of freedom, described by the angular variables (θ_i, ϕ_i) or equivalently by the unit vector $\hat{\mathbf{n}}_i$. The moment of inertia of an individual spherical ferromagnet is

$$I = \frac{2}{5}mR^2, \quad (18)$$

with $m = \frac{4}{3}\pi R^3\rho$. Importantly, the lattice construction does not alter the intrinsic dynamical parameters (μ, I) of each constituent particle. The extension from a single ferromagnet to a lattice increases the total polarized spin while preserving the intrinsic single-particle dynamical parameters of each constituent element. To make this separation explicit, it is useful to introduce collective angular variables corresponding to the spatially uniform ($k = 0$) mode, together with orthogonal combinations describing nonuniform ($k \neq 0$) modes. ULDM induces an effective magnetic-like field that is effectively uniform across the lattice scale. Consequently, the signal couples dominantly to the collective $k = 0$ mode. In contrast, inter-particle magnetic dipole-dipole interactions generate spatially varying internal fields that couple different sites and primarily excite nonuniform modes. This separation between collective and internal degrees of freedom underlies the possibility of coherent signal enhancement in the lattice while controlling many-body effects.

A ferromagnet lattice is not equivalent to a single larger ferromagnet containing the same total number of polarized spins. For a single spherical ferromagnet of radius R_{big} , the magnetic moment and moment of inertia scale as

$$\mu_{\text{big}} \propto R_{\text{big}}^3, \quad I_{\text{big}} \propto R_{\text{big}}^5. \quad (19)$$

Increasing the size therefore leads to a rapid growth of inertia, which suppresses the high-frequency dynamical response and limits the accessible bandwidth. By contrast, for a uni-

formly polarized configuration, the total magnetic moment magnitude scales as

$$|\mu_{\text{tot}}| \sim N|\mu|, \quad (20)$$

while each constituent retains its original moment of inertia I . The intrinsic susceptibility of each ferromagnet therefore remains unchanged, and the intrinsic single-particle dynamical bandwidth is not reduced simply by increasing N . The lattice enhances the total polarized spin participating in the measurement without introducing the dynamical penalties associated with scaling up a single rigid body.

An alternative architecture would be to allow the ferromagnetic particles to move freely in space, forming a gas-like ensemble rather than a fixed lattice. In principle, such a configuration could be stabilized against magnetic attraction by introducing additional electrostatic repulsion, for example by charging the particles to produce mutual Coulomb forces. While this approach can also prevent clustering, it introduces substantial dynamical complications. In a gas-like configuration, the relative positions of the ferromagnets fluctuate in time, leading to time-dependent dipole–dipole couplings. Collisions or close encounters between particles generate stochastic torques and momentum exchange, producing additional relaxation channels beyond those present in a fixed lattice. These processes result in collisional noise and dephasing, which degrade the coherence of collective motion. Moreover, in the absence of fixed equilibrium positions, the uniform ($k = 0$) collective mode is no longer dynamically protected. The center-of-mass and relative coordinates become coupled through interactions and external trapping forces, and the collective angular response mixes with translational and collisional degrees of freedom. As a consequence, the simple separation between collective signal enhancement and internal many-body dynamics, which is central to the lattice configuration, is lost. A fixed lattice architecture suppresses collisional processes, eliminates translational diffusion, and stabilizes the collective degrees of freedom. These features make the lattice configuration significantly more favorable than a gas-like ensemble for maximizing coherent signal accumulation.

B. Levitation and mechanical stability of the lattice

A central experimental requirement for realizing a ferromagnet lattice is the ability to stably levitate and spatially separate these magnetic particles to prevent mutual attraction

that causes clustering. In this section we discuss several possible levitation architectures and their suitability for constructing a stable lattice configuration.

Acoustic trapping. A natural and experimentally mature approach is acoustic levitation using ultrasonic standing-wave fields or phased-array transducers [12–15]. In such systems, pressure nodes provide restoring forces that confine small particles in three dimensions. By engineering multiple pressure nodes, one can generate a three-dimensional array of stable trapping sites with lattice constant a_0 . For micron-scale ferromagnets, the acoustic trapping force can readily exceed gravitational forces while remaining tunable independently of magnetic interactions. The restoring force scale can be written parametrically as

$$F_{\text{trap}} \sim k_{\text{trap}} \delta x, \quad (21)$$

where k_{trap} is the effective mechanical stiffness of the acoustic node. The magnetic dipole–dipole force between neighboring ferromagnets scales as

$$F_{\text{dd}} \sim \frac{\mu_0 |\mu|^2}{4\pi a_0^4}. \quad (22)$$

For experimentally realistic parameters, one can design k_{trap} such that $F_{\text{trap}} \gg F_{\text{dd}}$ over the relevant displacement range, ensuring mechanical stability of the lattice against dipolar attraction. Acoustic trapping therefore provides a flexible and scalable platform for arranging N ferromagnets over a spatial extent L_{lat} , while maintaining fixed equilibrium positions and suppressing translational diffusion. This architecture is well suited for room-temperature implementations.

Superconducting magnetic levitation. An alternative levitation strategy employs superconducting magnetic levitation, where Meissner screening currents provide vertical support [10]. While this method can achieve extremely low mechanical dissipation, it strongly constrains the geometry of the system. In particular, superconducting levitation typically stabilizes motion primarily along the vertical direction and restricts the allowable vertical separation between particles and the superconducting surface. The equilibrium levitation height is [10]

$$z_0 = \left(\frac{\mu_0 M^2 R^3}{16\rho g} \right)^{\frac{1}{4}}, \quad (23)$$

which is normally of the same order as R , and strongly limits the vertical extent of the lattice. Also, the magnetic field created by the ferromagnets at the surface of the superconductor is limited by the critical magnetic field of the superconductor, which limits the enlargement of

the lattice. For a lattice configuration extending over a macroscopic size L_{lat} , these geometric constraints make it difficult to realize a fully three-dimensional array of well-separated trapping sites. Furthermore, magnetic field gradients associated with superconducting screening may introduce spatial inhomogeneities in the local magnetic environment across the lattice. For these reasons, although superconducting levitation is highly attractive for single-particle experiments, it is less suitable for constructing an extended ferromagnet lattice and is not the preferred architecture in the present context.

Optical levitation and vacuum operation. Optical trapping provides another viable route to constructing a ferromagnet lattice. Optical tweezers or optical standing-wave traps can generate arrays of stable trapping sites with precise spatial control [16]. In contrast to acoustic trapping, optical levitation is naturally compatible with high-vacuum environments that offer several advantages. The absence of air eliminates collisional damping, reduces thermal noise acting on the rotational degrees of freedom, and provides an ideal mechanical isolation from the environment. Reduced thermal load improves long-term stability and may enable long-term integration. In practice, this approach faces substantial technical challenges. Ferromagnetic materials generally exhibit strong optical absorption and scattering at typical trapping wavelengths, leading to enhanced radiation-pressure imbalance and significant internal heating. These effects compromise trap stability and can degrade magnetic properties, posing a limitation for low-noise operation [17–19]. Nevertheless, recent developments in optical manipulation of mesoscopic objects suggest that lattice-scale implementations are feasible in principle [17, 20, 21].

Conventional magnetic levitation. Conventional magnetic levitation using static magnetic field gradients may also be considered. Earnshaw’s theorem prohibits stable levitation of a purely ferromagnetic particle in static magnetic fields alone; however, dynamic stabilization techniques or hybrid magnetic–mechanical schemes can provide effective confinement. In practice, magnetic levitation of multiple ferromagnets arranged in a regular lattice would require carefully engineered field configurations to prevent cross-coupling between sites. Moreover, magnetic gradients used for translational confinement may interfere with the controlled magnetic environment required for precision ULDM searches. As a result, while magnetic levitation is feasible for small numbers of particles, scaling to large N with uniform trapping properties across a large size is technically demanding.

Regardless of the specific levitation architecture, the essential requirement is that trans-

lational restoring forces dominate magnetic dipole–dipole attraction. Provided that

$$k_{\text{trap}}a_0 \gg \frac{\mu_0|\mu|^2}{4\pi a_0^4}, \quad (24)$$

the equilibrium lattice remains mechanically stable and resistant to collapse. Since the trapping stiffness can be tuned independently of the magnetic properties of the ferromagnets, there exists a broad experimental parameter window in which a stable lattice of N levitated ferromagnets can be realized over a macroscopic scale.

IV. INTERACTION-INDUCED MODIFICATION OF THE LATTICE RESPONSE

We now turn to the modification of the coherent lattice response induced by magnetic dipole-dipole interactions. For a single levitated ferromagnet, the linear response to a weak magnetic field is fully characterized by the susceptibility matrix $\chi(\omega)$ derived in Sec. II. In a lattice, however, each ferromagnet also experiences the magnetic field generated by all the others. The resulting dipole-dipole interaction couples different sites and turns the problem into a genuine many-body response problem. Even when the interaction is sufficiently weak not to qualitatively alter the order of magnitude of the response, it can still reshape the spectral structure by shifting the collective modes and mixing the uniform response with nonuniform lattice modes. A controlled treatment of these effects is therefore necessary before discussing the final detector noise.

The analysis naturally proceeds in two steps. We first consider an ideal periodic lattice, for which translational invariance allows the dynamics to be diagonalized in reciprocal space. This provides the unperturbed collective-mode structure and shows explicitly that a spatially uniform external field couples only to the $\mathbf{k} = 0$ mode. We then incorporate finite-boundary effects, which break translational invariance and induce mode mixing between the coherent channel and modes with $\mathbf{k} \neq 0$. This boundary-induced mixing will be the key mechanism responsible for the interaction correction to the observable response.

A. Lattice dynamics in reciprocal space

We begin from the linear response of an individual ferromagnet in the fully trapped regime. For compactness, we denote by $\delta\mathbf{n}_i(\omega)$ the two-component angular response of

the i th ferromagnet in the transverse plane. In the absence of inter-particle coupling, the response is simply

$$\delta \mathbf{n}_i(\omega) = -\mu \chi(\omega) \mathbf{B}_{\text{ext}}(\omega), \quad (25)$$

where μ is the magnetic moment and \mathbf{B}_{ext} is assumed to be approximately uniform across the lattice.

In the lattice, each ferromagnet is additionally driven by the magnetic field produced by all other ferromagnets. For a pair of sites i and j separated by $\mathbf{r}_{ij} = \mathbf{r}_i - \mathbf{r}_j$, the dipole field can be written in terms of the standard dipolar tensor. Restricting to the two transverse angular components relevant to the linearized dynamics, we write the interaction-induced field on site i as

$$\mathbf{B}_i^{\text{int}}(\omega) = B_{\text{dd}} \sum_{j \neq i} T_{ij} \delta \mathbf{n}_j(\omega), \quad (26)$$

where

$$B_{\text{dd}} \equiv \frac{\mu_0 |\mu|}{4\pi a_0^3} \quad (27)$$

sets the characteristic dipolar field scale for lattice spacing a_0 , and the dimensionless interaction kernel is

$$T_{ij} = \frac{a_0^3}{r_{ij}^3} \begin{pmatrix} 1 - 3\hat{r}_{ij,x}^2 & -3\hat{r}_{ij,x}\hat{r}_{ij,y} \\ -3\hat{r}_{ij,x}\hat{r}_{ij,y} & 1 - 3\hat{r}_{ij,y}^2 \end{pmatrix}. \quad (28)$$

Here $\hat{r}_{ij,a} \equiv r_{ij,a}/r_{ij}$ denotes the a th component of the unit vector along the bond, and we set $T_{ii} = 0$ to exclude self-interactions. The equation of motion of the lattice then becomes

$$\delta \mathbf{n}_i(\omega) = -\mu \chi(\omega) [\mathbf{B}_{\text{ext}}(\omega) + \mathbf{B}_i^{\text{int}}(\omega)]. \quad (29)$$

Substituting Eq. (26) into Eq. (29) and rearranging gives the coupled linear system

$$\sum_j [\chi^{-1}(\omega)\delta_{ij} + \mu B_{\text{dd}} T_{ij}] \delta \mathbf{n}_j(\omega) = -\mu \mathbf{B}_{\text{ext}}(\omega), \quad (30)$$

where the external field is assumed uniform, so the source term is site independent. This equation is exact within the linear-response regime. Compared with the single-ferromagnet problem, the only new ingredient is the dipolar kernel T_{ij} , which couples the responses of different lattice sites.

For an ideal periodic lattice, the interaction kernel depends only on the relative displacement between sites, and the problem can therefore be diagonalized in reciprocal space. We

introduce

$$\delta \mathbf{n}_i(\omega) = \frac{1}{N} \sum_{\mathbf{k}} e^{i\mathbf{k}\cdot\mathbf{r}_i} \mathbf{u}_{\mathbf{k}}(\omega), \quad (31)$$

where N is the total number of ferromagnets and \mathbf{k} runs over the reciprocal lattice. The Fourier transform of the interaction kernel is defined by

$$T(\mathbf{k}) = \sum_{j \neq i} e^{-i\mathbf{k}\cdot(\mathbf{r}_i - \mathbf{r}_j)} T_{ij}, \quad (32)$$

which depends only on the relative displacement and is therefore diagonal in reciprocal space. Equation (30) then reduces to

$$[\chi^{-1}(\omega) + \mu B_{\text{dd}} T(\mathbf{k})] \mathbf{u}_{\mathbf{k}}(\omega) = -\mu \mathbf{B}_{\text{ext}}(\omega) \delta_{\mathbf{k},0}. \quad (33)$$

It is therefore natural to define the interaction-modified susceptibility matrix

$$\chi_{\text{mod}}^{-1}(\omega, \mathbf{k}) \equiv \chi^{-1}(\omega) + \mu B_{\text{dd}} T(\mathbf{k}). \quad (34)$$

The many-body problem in the ideal periodic lattice is thus reduced to a set of independent 2×2 response problems labeled by \mathbf{k} . The role of the dipole-dipole interaction is to renormalize the susceptibility differently for different lattice modes, thereby shifting and reshaping the collective spectrum.

A crucial consequence of Eq. (33) is that a spatially uniform external field couples only to the $\mathbf{k} = 0$ mode. In the ideal periodic limit, all modes with $\mathbf{k} \neq 0$ remain unexcited under uniform driving, and the observable response is entirely governed by the coherent channel,

$$\mathbf{u}_0(\omega) = -\mu \chi_{\text{mod}}(\omega, \mathbf{0}) \mathbf{B}_{\text{ext}}(\omega). \quad (35)$$

At this stage, the lattice behaves as a coherent sum of identical ferromagnets with a susceptibility renormalized by the interaction. No mode mixing occurs, and the response is fully governed by the coherent channel. The situation changes once translational invariance is broken. In a finite lattice, the boundary introduces a nonperiodic correction to the dipolar kernel, so that the reciprocal-space modes are no longer exact eigenmodes of the dynamics. As a result, the coherent $\mathbf{k} = 0$ response is mixed with modes at $\mathbf{k} \neq 0$, and the observable susceptibility acquires an additional correction beyond the ideal periodic result. We analyze this boundary-induced mode mixing in the next subsection.

B. Boundary-induced mode mixing and effective coherent response

The simplification obtained in the previous subsection relies entirely on translational invariance. In a finite lattice, this symmetry is broken by the boundary, and the reciprocal-lattice modes are no longer exact eigenmodes of the dynamics. Physically, this means that even under a spatially uniform drive, the coherent $\mathbf{k} = 0$ response can leak into modes with $\mathbf{k} \neq 0$, which then feed back into the observable response of the lattice. The boundary effect therefore does not merely shift the collective spectrum but mixes the coherent channel with nonuniform lattice modes.

To make this structure explicit, we decompose the full interaction kernel into a translationally invariant part and a boundary correction,

$$T_{\text{tot}} = T + T_{\text{bnd}}. \quad (36)$$

Here T denotes the part that can still be diagonalized in reciprocal space, while T_{bnd} contains the nonperiodic correction induced by the finite boundary. The diagonal part of T_{bnd} in reciprocal space can be absorbed into the definition of the interaction-modified susceptibility. After this redefinition, T_{bnd} is understood as the off-diagonal component responsible for mode mixing.

Since the experimentally relevant signal is the coherent response under a nearly uniform external field, it is useful to introduce the coherent channel

$$|0\rangle \equiv \frac{1}{N}(1, 1, \dots, 1)^T, \quad (37)$$

which represents the uniform lattice mode. The measured response is the projection of the full lattice motion onto this channel. Formally, the coherent response can be written as

$$\mathbf{u}_{\text{coh}}(\omega) \equiv \langle 0 | \mathbf{u}(\omega) = -\mu \langle 0 | [\chi^{-1}(\omega) + \mu B_{\text{dd}} T_{\text{tot}}]^{-1} | 0 \rangle \mathbf{B}_{\text{ext}}(\omega), \quad (38)$$

where \mathbf{u} denotes the full lattice response vector in site space. Using the reciprocal-lattice basis as a complete basis for the lattice degrees of freedom, the equation of motion may be rewritten in mode space as

$$\sum_{\mathbf{k}} \left[\chi_{\text{mod}}^{-1}(\omega, \mathbf{k}) \mathbf{u}_{\mathbf{k}}(\omega) |\mathbf{k}\rangle + \mu B_{\text{dd}} \sum_{\mathbf{q}} V_{\mathbf{kq}} \mathbf{u}_{\mathbf{q}}(\omega) |\mathbf{k}\rangle \right] = -\mu \mathbf{B}_{\text{ext}}(\omega) |0\rangle, \quad (39)$$

where

$$V_{\mathbf{kq}} \equiv \langle \mathbf{k} | T_{\text{bnd}} | \mathbf{q} \rangle \quad (40)$$

is the boundary-induced mode-mixing matrix element. In the absence of T_{bnd} , one has $V_{\mathbf{k}\mathbf{q}} = 0$ and the modes remain decoupled, recovering the ideal periodic result derived in Sec. IV.A. The entire effect of the finite boundary is therefore encoded in the off-diagonal matrix $V_{\mathbf{k}\mathbf{q}}$. Projecting Eq. (39) onto $|\mathbf{k}\rangle$ gives

$$\chi_{\text{mod}}^{-1}(\omega, \mathbf{k}) \mathbf{u}_{\mathbf{k}} + \mu B_{\text{dd}} \sum_{\mathbf{q} \neq \mathbf{k}} V_{\mathbf{k}\mathbf{q}} \mathbf{u}_{\mathbf{q}} = -\mu \mathbf{B}_{\text{ext}} \delta_{\mathbf{k},0}. \quad (41)$$

For $\mathbf{k} \neq 0$, these modes are not directly driven by the uniform external field; they are populated only through boundary-induced coupling to other modes, ultimately originating from the coherent mode. Their response may therefore be viewed as virtual leakage channels that renormalize the $\mathbf{k} = 0$ dynamics.

When the leakage into nonuniform modes remains perturbative, so that the dynamics is still governed primarily by the coherent channel, one may solve Eq. (41) iteratively. To leading nontrivial order, the $\mathbf{k} \neq 0$ modes are induced by the coherent mode according to

$$\mathbf{u}_{\mathbf{k}} \simeq -\mu B_{\text{dd}} \chi_{\text{mod}}(\omega, \mathbf{k}) V_{\mathbf{k}0} \mathbf{u}_0, \quad \mathbf{k} \neq 0. \quad (42)$$

Substituting this back into the $\mathbf{k} = 0$ equation yields an effective equation of motion for the coherent response,

$$[\chi_{\text{mod}}^{-1}(\omega, \mathbf{0}) - \Sigma_{\text{bnd}}(\omega)] \mathbf{u}_0 = -\mu \mathbf{B}_{\text{ext}}. \quad (43)$$

Here

$$\Sigma_{\text{bnd}}(\omega) \equiv |\mu|^2 B_{\text{dd}}^2 \sum_{\mathbf{k} \neq 0} V_{0\mathbf{k}} \chi_{\text{mod}}(\omega, \mathbf{k}) V_{\mathbf{k}0} \quad (44)$$

is the self-energy induced by the boundary correction.

Equation (43) is the central result of this subsection. It shows that, after integrating out the nonuniform modes, the observable coherent response retains the same form as in the ideal lattice, but with an additional self-energy correction generated by virtual excursions into $\mathbf{k} \neq 0$ modes. The boundary therefore plays the role of a mode-mixing perturbation: it does not create an independent collective mode by itself, but modifies the coherent response through coupling to the existing spectrum of nonuniform lattice modes. The corrected coherent susceptibility can thus be written as

$$\chi_{\text{coh}}^{-1}(\omega) = \chi_{\text{mod}}^{-1}(\omega, \mathbf{0}) - \Sigma_{\text{bnd}}(\omega), \quad (45)$$

so that

$$\mathbf{u}_0(\omega) = -\mu \chi_{\text{coh}}(\omega) \mathbf{B}_{\text{ext}}(\omega). \quad (46)$$

This form reduces the full finite-lattice problem to an effective response theory for the coherent channel alone. All boundary effects are encoded in the frequency-dependent matrix $\Sigma_{\text{bnd}}(\omega)$.

The physical meaning of Eq. (44) is transparent. The factor $V_{0\mathbf{k}}$ describes the boundary-induced leakage of the coherent mode into a nonuniform mode \mathbf{k} , while $\chi_{\text{mod}}(\omega, \mathbf{k})$ governs the response of that intermediate mode under the interaction-modified lattice dynamics. The factor $V_{\mathbf{k}0}$ then describes the coupling of this amplitude back into the coherent channel. The boundary correction is therefore controlled both by the strength of the mode mixing and by the susceptibility of the intermediate nonuniform modes. Even when the boundary itself is weak, its effect can be enhanced if some $\mathbf{k} \neq 0$ modes are close to singular response. This structure will be important for identifying the parameter regime in which the perturbative treatment remains valid.

For later convenience, it is useful to introduce a dimensionless form of the self-energy. Writing

$$\chi_{\text{mod}}^{-1}(\omega, \mathbf{k}) = X_0 \xi(\omega, \mathbf{k}), \quad (47)$$

where $X_0 = I\omega_I v_{\theta\theta}$ sets the overall susceptibility scale and $\xi(\omega, \mathbf{k})$ is dimensionless. The matrix ξ is normalized so that its entries are simply 1 and $v_{\phi\phi}/v_{\theta\theta}$ in the absence of interaction. One obtains

$$\sigma_{\text{bnd}}(\omega) \equiv \frac{1}{X_0} \Sigma_{\text{bnd}}(\omega) = \lambda_{\text{int}}^2 \sum_{\mathbf{k} \neq 0} V_{0\mathbf{k}} \xi^{-1}(\omega, \mathbf{k}) V_{\mathbf{k}0}, \quad (48)$$

with

$$\lambda_{\text{int}} = \frac{R^3 \omega_s}{3a_0^3 v_{\theta\theta}} \quad (49)$$

a dimensionless parameter characterizing the interaction strength. Here

$$\omega_s = \gamma_e \mu_0 M \quad (50)$$

is a material-dependent frequency scale set by the magnetization M of the ferromagnet. In this form, the boundary correction is naturally separated into three ingredients: the overall interaction scale λ_{int}^2 , the geometric mode-mixing matrix elements $V_{0\mathbf{k}}$, and the intrinsic lattice response $\xi^{-1}(\omega, \mathbf{k})$.

C. Perturbative regime, near-singular modes, and beyond

The effective coherent susceptibility derived above provides a compact description of the boundary correction. However, this description is valid only when the leakage from the coherent channel into nonuniform modes remains perturbative. We now examine the regime in which this assumption is valid, and identify the physical mechanism that can enhance the boundary effect.

To obtain Eq. (42) from Eq. (41), one assumes that, on the right-hand side of the formal solution, the dominant source term is the direct boundary-induced mixing with the coherent mode, while the feedback from other nonuniform modes remains subleading. In other words, the nonuniform modes are assumed to be slaved to the coherent response rather than forming an independent strongly mixed sector. Under this approximation,

$$\mathbf{u}_{\mathbf{k}} \simeq -\mu B_{\text{dd}} \chi_{\text{mod}}(\omega, \mathbf{k}) V_{\mathbf{k}0} \mathbf{u}_0, \quad \mathbf{k} \neq 0. \quad (51)$$

The validity of this approximation should be checked self-consistently. Substituting the leading-order expression Eq. (51) back into Eq. (41), one finds that the contribution generated by mode-to-mode feedback among the nonuniform sector is small only if

$$\left\| -\mu B_{\text{dd}} \sum_{\mathbf{q} \neq 0, \mathbf{k}} V_{\mathbf{k}\mathbf{q}} \chi_{\text{mod}}(\omega, \mathbf{q}) V_{\mathbf{q}0} \right\| \ll \|V_{\mathbf{k}0}\|, \quad \mathbf{k} \neq 0. \quad (52)$$

This is the direct self-consistency condition for the coherent-mode-dominance approximation. It states that the secondary leakage path $0 \rightarrow \mathbf{q} \rightarrow \mathbf{k}$ must remain small compared with the primary leakage path $0 \rightarrow \mathbf{k}$. Only in this regime can the nonuniform modes be integrated out perturbatively to produce the boundary self-energy of the coherent channel.

This condition has two distinct physical implications. The first is the intuitive one: the interaction should not be too strong overall. If the dipolar interaction scale becomes too large, then the boundary-induced couplings are no longer a small perturbation on top of the unperturbed lattice modes, and the entire nonuniform sector can become strongly hybridized. In that regime, the response is no longer organized around a dominant coherent mode, and the perturbative elimination of $\mathbf{k} \neq 0$ modes breaks down globally. At a qualitative level, one therefore expects the coherent-mode-dominance approximation to remain viable when λ_{int} is not too large, typically $\lambda_{\text{int}} \lesssim 0.1$ up to geometry- and frequency-dependent corrections.

The second implication is more subtle but more important for the present system. Even when the overall interaction strength is moderate, the self-consistency condition can still fail

if some nonuniform modes acquire an anomalously large susceptibility. This occurs when the matrix $\chi_{\text{mod}}^{-1}(\omega, \mathbf{k})$ develops a small eigenvalue, or equivalently when the dimensionless matrix $\xi(\omega, \mathbf{k})$ introduced in Eq. (47) becomes nearly singular. In that case, the response of the intermediate mode \mathbf{q} is strongly enhanced, and the secondary leakage process in Eq. (52) is no longer suppressed. To make this point explicit, let $\nu_\alpha(\omega, \mathbf{k})$ denote the eigenvalues of $\xi(\omega, \mathbf{k})$. Then the induced amplitude of a nonuniform mode contains contributions weighted by $1/\nu_\alpha(\omega, \mathbf{k})$. Therefore, even if the geometric mixing matrix elements $V_{\mathbf{kq}}$ are small, the corresponding correction can become large when one or more $\nu_\alpha(\omega, \mathbf{k})$ approach zero. The breakdown of the approximation is then not driven by a parametrically large boundary term, but by the strong response of a subset of near-singular modes. Physically, the boundary opens a leakage channel from the coherent mode into the nonuniform sector, and the near-singular modes amplify this leakage by providing almost resonant intermediate states.

It is useful to distinguish these two mechanisms conceptually. The first is a global strong-coupling effect: the interaction strength itself is so large that no perturbative treatment around the coherent mode is justified. The second is a local spectral effect: the interaction is still moderate in a bulk sense, but the lattice contains exceptional modes at specific frequencies for which the response is strongly enhanced. In the present problem, the latter is the more relevant mechanism. Over much of the spectrum, the coherent-mode picture remains valid and the interaction correction is smooth. The main source of irregular behavior is instead the presence of near-singular modes, which distort the coherent susceptibility over a restricted frequency range through enhanced boundary-induced mixing.

When the approximation fails, the relevant near-singular modes must be retained explicitly rather than integrated out perturbatively. A convenient way to proceed is to divide the full momentum space into two parts: a subspace \mathcal{S} containing the near-singular modes and the coherent mode, and the remaining regular modes. The regular modes continue to contribute perturbatively through the same self-energy structure as before, while the modes in \mathcal{S} are treated on equal footing with the coherent mode. After excluding the modes in \mathcal{S} from the perturbative treatment, the coherent-mode-dominance condition is replaced by

$$\left\| \sum_{\mathbf{q} \notin \mathcal{S}} V_{\mathbf{kq}} \mathbf{u}_{\mathbf{q}} \right\| \ll \|V_{\mathbf{k}0} \mathbf{u}_0\|. \quad (53)$$

That is, once the near-singular modes have been separated out, the residual modes outside this subset must still remain weakly coupled in the same sense as before. The subset \mathcal{S}

therefore plays a role analogous to a near-degenerate subspace: instead of solving directly for u_0 alone, one solves the coupled equations within this subspace. Nevertheless, the choice of the subspace \mathcal{S} is not unique. In principle, one may enlarge \mathcal{S} to improve the accuracy of the treatment, at the cost of solving a correspondingly larger set of coupled linear equations involving the matrix elements $V_{\mathbf{k}\mathbf{q}}$.

The amplitudes of modes outside the subset can then be fully expressed in terms of the amplitudes of the modes inside the subset,

$$\mathbf{u}_{\mathbf{k}} = \xi^{-1}(\omega, \mathbf{k}) \sum_{\mathbf{s} \in \mathcal{S}} \lambda_{\text{int}} V_{\mathbf{k}\mathbf{s}} \mathbf{u}_{\mathbf{s}}, \quad \mathbf{k} \notin \mathcal{S}. \quad (54)$$

Substituting this relation back into the equations of motion, one obtains

$$\sum_{\mathbf{s}' \in \mathcal{S}} [\xi(\omega, \mathbf{s}') \delta_{\mathbf{s}', \mathbf{s}} - \lambda_{\text{int}} V_{\mathbf{s}', \mathbf{s}}] \mathbf{u}_{\mathbf{s}} = 0, \quad \text{for } \mathbf{s} \in \mathcal{S} \text{ and } \mathbf{s} \neq 0, \quad (55)$$

and

$$\xi(\omega, 0) \mathbf{u}_0 - \lambda_{\text{int}} \sum_{\mathbf{s} \in \mathcal{S}} \left[V_{0\mathbf{s}} + \lambda_{\text{int}} \sum_{\mathbf{k} \notin \mathcal{S}} V_{0\mathbf{k}} \xi^{-1}(\omega, \mathbf{k}) V_{\mathbf{k}\mathbf{s}} \right] \mathbf{u}_{\mathbf{s}} = -\frac{\mu B_{\text{ext}}}{X_0}. \quad (56)$$

The modes outside the subset \mathcal{S} also generate a self-energy correction for each mode inside \mathcal{S} . However, by construction, all potentially singular modes have already been removed from this residual self-energy. The remaining contribution is therefore expected to remain small compared with the direct coupling term $V_{0\mathbf{s}}$ and may be neglected to leading order. Treating this as a partitioned matrix equation, the solution for the coherent response becomes

$$\chi'_{\text{coh}}(\omega) = \frac{1}{X_0} [\xi(\omega, 0) - \sigma'_{\text{bnd}}(\omega)]^{-1}, \quad (57)$$

where the dimensionless self-energy is

$$\sigma'_{\text{bnd}}(\omega) = \lambda_{\text{int}}^2 \left[\sum_{\mathbf{s}, \mathbf{s}' \in \mathcal{S} \setminus \{0\}} V_{0\mathbf{s}} G_{\mathbf{s}, \mathbf{s}'}(\omega) V_{\mathbf{s}'0} + \sum_{\mathbf{k} \notin \mathcal{S}} V_{0\mathbf{k}} \xi^{-1}(\omega, \mathbf{k}) V_{\mathbf{k}0} \right], \quad (58)$$

and

$$G_{\mathbf{s}, \mathbf{s}'}^{-1}(\omega) = \xi(\omega, \mathbf{s}') \delta_{\mathbf{s}', \mathbf{s}} - \lambda_{\text{int}} V_{\mathbf{s}', \mathbf{s}} \quad (59)$$

is the response matrix of the near-singular subset excluding the coherent mode. In other words, once the near-singular modes are retained explicitly, the effect of the boundary has the same formal structure as before, except that the simple susceptibility of an isolated intermediate mode is replaced by the full response matrix of the near-singular subset. This expression reduces to the perturbative result in Sec. IV.B when the subset \mathcal{S} is empty or when the couplings among the retained modes may be neglected.

D. Small- \mathbf{k} structure of the interaction kernel

The analysis above shows that the boundary correction is most strongly enhanced when the coherent mode couples to nonuniform modes with anomalously large susceptibility. To identify where such near-singular modes arise, we now examine the structure of the interaction kernel $T(\mathbf{k})$ for a simple cubic lattice. Its reciprocal lattice is again simple cubic, with a minimum wave number

$$k_0 = \frac{2\pi}{L_{\text{lat}}}, \quad (60)$$

where L_{lat} is the linear size of the lattice. There is no simple closed-form expression for the full lattice interaction kernel in reciprocal space. We focus on its small- \mathbf{k} behavior, which is the most relevant regime for the boundary correction. Physically, this is because the boundary correction is concentrated near the edge of the lattice in real space, and therefore couples predominantly to long-wavelength modes in reciprocal space.

According to the Ewald summation method, the dipolar interaction of the discrete lattice can be decomposed into a long-range continuum contribution and a short-range discrete correction [22, 23]. The long-range part can be Fourier transformed analytically as in continuum space, while the short-range part contributes only regular corrections. In the limit $ka_0 \ll 1$, the interaction kernel takes the form

$$T(\mathbf{k}) = 4\pi \begin{pmatrix} \hat{k}_x^2 - \frac{1}{3} & \hat{k}_x \hat{k}_y \\ \hat{k}_x \hat{k}_y & \hat{k}_y^2 - \frac{1}{3} \end{pmatrix} + \mathcal{O}[(ka_0)^2], \quad (61)$$

where $\hat{\mathbf{k}} = \mathbf{k}/k$ is the unit vector along \mathbf{k} . The leading term in Eq. (61) is nonanalytic: it depends only on the direction of \mathbf{k} , but not on its magnitude. This is a direct consequence of the long-range nature of the dipole-dipole interaction. As a result, a family of modes with different $|\mathbf{k}|$ but nearly the same direction share the same leading interaction energy, and therefore nearly the same self-energy correction. The near-singular modes therefore appear in directional groups rather than as isolated points in momentum space. Consequently, once a near-singular direction exists, a whole set of nearby long-wavelength modes can become strongly enhanced, making the response particularly sensitive to the boundary-induced mode mixing.

Using Eq. (61), one can obtain the eigenvalues of the dimensionless modified susceptibility

matrix ξ in the small- \mathbf{k} approximation,

$$\nu_1 = 1 - \bar{\omega}^2 + \frac{4\pi}{3}\lambda_{\text{int}}, \quad (62)$$

$$\nu_2 = 1 - \bar{\omega}^2 - 4\pi\lambda_{\text{int}}\left(\frac{2}{3} - \hat{k}_z^2\right), \quad (63)$$

where

$$\bar{\omega} = \frac{\omega}{\sqrt{\omega_T v_{\theta\theta}}} \quad (64)$$

is the dimensionless frequency, with $\bar{\omega} = 1$ corresponding to the reference single-particle resonance frequency set by $v_{\theta\theta}$. Here we specify the fully trapped regime where the single-particle susceptibility is approximately diagonal. The first eigenvalue ν_1 is independent of \mathbf{k} , whereas the second one ν_2 retains the directional dependence through \hat{k}_z . The first branch therefore produces a uniform interaction shift in the small- \mathbf{k} limit, while the second branch is anisotropic and can approach zero along particular directions. The anisotropic near-singular structure discussed in the previous subsection is therefore expected to originate primarily from this second branch. In particular, once the frequency is tuned such that ν_2 becomes small for some direction $\hat{\mathbf{k}}$, all sufficiently small- k modes along nearby directions acquire similarly large responses and contribute coherently to the boundary self-energy. As $\hat{k}_z \in [0, 1]$, these two eigenvalues together determine a frequency band

$$\bar{\omega} \in \left[\sqrt{\max\left(1 - \frac{8\pi}{3}\lambda_{\text{int}}, 0\right)}, \sqrt{1 + \frac{4\pi}{3}\lambda_{\text{int}}} \right], \quad (65)$$

and near-singular modes can only exist within this frequency band.

E. Boundary correction formalism and numerical results

The ideal interaction kernel $T(\mathbf{k})$ discussed above corresponds to an infinite lattice with periodic boundary conditions. For the numerical treatment of a finite lattice, we adopt an operational decomposition: the diagonal part of the finite-lattice kernel in reciprocal space is identified as $T(\mathbf{k})$, while the residual off-diagonal part is treated as the boundary-induced mixing term. This definition coincides with the ideal bulk kernel only in the infinite-lattice limit. For a finite lattice, the translational symmetry is broken by the boundary, and the actual interaction kernel is obtained by restricting the ideal kernel to the occupied region

of the lattice. Let the finite lattice occupy a spatial region D , and define the occupation function

$$s(\mathbf{r}) = \begin{cases} 1, & \mathbf{r} \in D, \\ 0, & \mathbf{r} \notin D. \end{cases} \quad (66)$$

Correspondingly, we introduce the projection operator

$$S = \sum_{\mathbf{r}} s(\mathbf{r}) |\mathbf{r}\rangle \langle \mathbf{r}|. \quad (67)$$

The interaction kernel of the finite lattice is then

$$T^{\text{finite}} = STS. \quad (68)$$

In reciprocal space, this becomes

$$T_{\mathbf{k}\mathbf{q}}^{\text{finite}} = \sum_{\mathbf{p}} \tilde{S}(\mathbf{p} - \mathbf{k}) T(\mathbf{p}) \tilde{S}(\mathbf{q} - \mathbf{p}), \quad (69)$$

where

$$\tilde{S}(\mathbf{q} - \mathbf{k}) \equiv \langle \mathbf{k} | S | \mathbf{q} \rangle = \frac{1}{N} \sum_{\mathbf{r}} s(\mathbf{r}) e^{i(\mathbf{q} - \mathbf{k}) \cdot \mathbf{r}} \quad (70)$$

is the Fourier transform of the occupation function. The corresponding boundary correction is therefore

$$V_{\mathbf{k}\mathbf{q}} = \sum_{\mathbf{p}} \tilde{S}(\mathbf{p} - \mathbf{k}) T(\mathbf{p}) \tilde{S}(\mathbf{q} - \mathbf{p}) - \delta_{\mathbf{k}\mathbf{q}} T(\mathbf{k}). \quad (71)$$

In an infinite periodic lattice, \tilde{S} reduces to a Kronecker delta and the kernel remains diagonal in \mathbf{k} space. In a finite lattice, however, the window function \tilde{S} broadens the momentum support and couples different reciprocal-space modes. The boundary correction is precisely the off-diagonal part generated by this finite-size projection. Note that, in general, the diagonal kernel $T(\mathbf{k})$ defined here is not identical to that of the infinite lattice, since the boundary correction also contributes nonzero diagonal terms that have been absorbed into the definition of $T(\mathbf{k})$.

To evaluate the boundary correction quantitatively, we numerically construct a $100 \times 100 \times 100$ simple cubic lattice, build the interaction kernel in real space, and Fourier transform it to obtain the exact kernel in reciprocal space. We then separate the diagonal and off-diagonal parts of the finite-lattice kernel. The diagonal part is identified with $T(\mathbf{k})$ and used to define the modified susceptibility of each mode, while the residual off-diagonal part is identified with T_{bnd} , so that by construction

$$V_{\mathbf{k}\mathbf{k}} = 0. \quad (72)$$

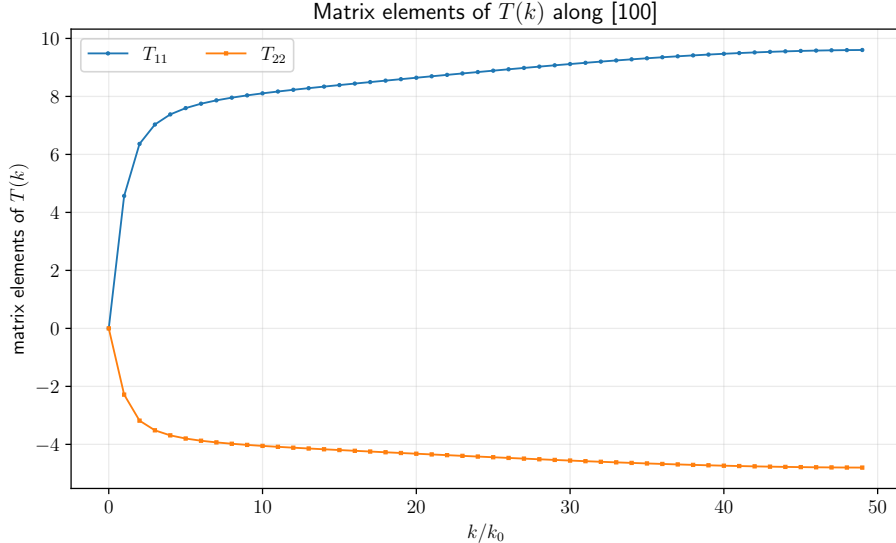


FIG. 1. Diagonal components of the interaction kernel $T(\mathbf{k})$ extracted numerically for a $100 \times 100 \times 100$ simple cubic lattice, shown along the $\mathbf{k} \parallel (1, 0, 0)$ direction. In the small- k regime, the result agrees with the analytical long-wavelength expression of the ideal lattice. The sharp tendency toward zero at the smallest k is caused by the finite-size window function rather than by the bulk interaction itself.

FIG. 1 shows the diagonal components of the numerically extracted kernel along the $\mathbf{k} \parallel (1, 0, 0)$ direction. In the small- k region, the result agrees well with the analytical expression obtained for the ideal lattice in Sec. IV.D. The sharp tendency toward zero at the smallest accessible k is a finite-size effect originating from the window function $\tilde{S}(\mathbf{q})$, and does not reflect the bulk interaction kernel of the infinite system. FIG. 2 shows the numerical value of $V_{0\mathbf{k}}$ along the three high-symmetry directions. It is clear that the dominant contribution is concentrated at small k , confirming that the boundary couples the coherent mode most strongly to long-wavelength nonuniform modes.

With the finite-lattice kernel determined numerically, we next evaluate the boundary self-energy and the resulting coherent susceptibility. In the following calculations, we take $\lambda_{\text{int}} = 0.0665$. In the perturbative regime, the self-energy is obtained from Eq. (44), while in the presence of near-singular modes the corresponding generalized expression Eq. (58) is used. In both cases, the physical content is the same: the coherent response is renormalized by virtual leakage into nonuniform modes and the subsequent return to the coherent channel. The numerical result for the self-energy is shown in FIG. 3. Within the frequency interval

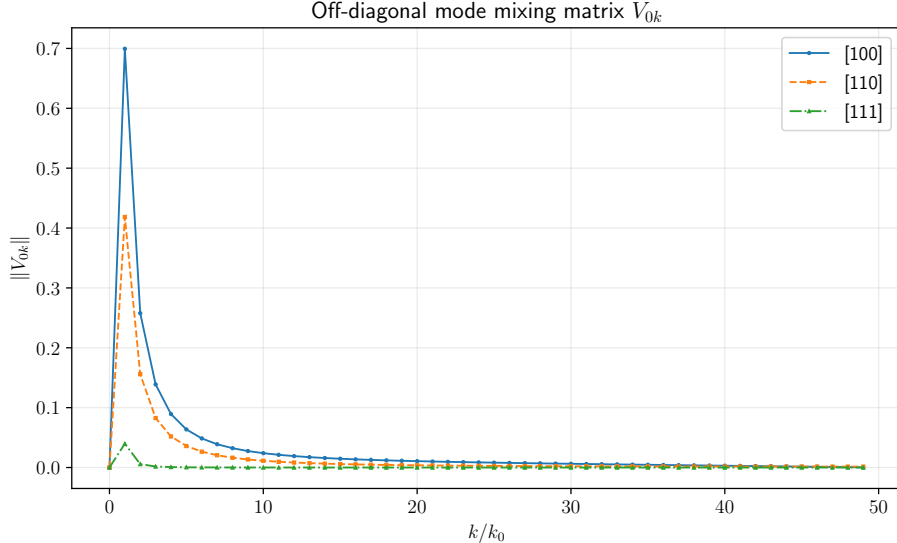


FIG. 2. Boundary-induced mode-mixing amplitude $V_{0\mathbf{k}}$ along the three high-symmetry directions of the simple cubic lattice. The dominant weight is concentrated in the small- k region, showing that the coherent mode couples most strongly to long-wavelength nonuniform modes.

Eq. (65), the self-energy develops a sequence of small peaks associated with individual discrete \mathbf{k} modes. Each of these peaks is approximately antisymmetric about its center, with one positive and one negative side. Among them, two dominant peaks stand out as the main deviations from zero. The first one is associated with the near-singular point of the $\mathbf{k} = (k_0, 0, 0)$ mode. Since this mode has the largest boundary mixing amplitude $V_{0\mathbf{k}}$, it gives rise to the highest individual peak. The second dominant structure is associated approximately with the point where the eigenvalue ν_1 , which is constant in the small- k approximation, approaches zero. In this case, a large number of momentum modes become nearly singular simultaneously, producing the strongest enhancement over the entire frequency range.

The resulting corrected coherent susceptibility is compared with the bare coherent susceptibility in FIG. 4. As anticipated from the preceding analysis, the boundary correction does not produce a simple overall suppression of the response. Instead, it introduces a structured frequency dependence through the coupling to long-wavelength nonuniform modes. Over most of the spectrum the correction remains moderate, but near frequencies where the small- k sector approaches a singular response, the susceptibility is visibly distorted by the enhanced mode mixing. This behavior is precisely the finite-size manifestation of the near-singular directional structure discussed in Sec. IV.D.

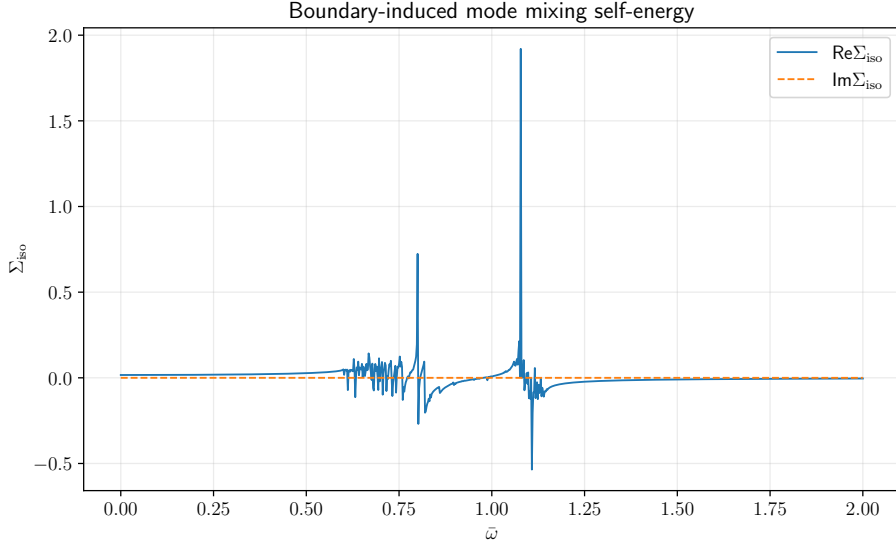


FIG. 3. Boundary-induced self-energy of the coherent mode, calculated for the finite simple cubic lattice. The dominant contribution comes from long-wavelength nonuniform modes coupled to the coherent channel by the boundary. The vertical axis is shown on a symmetric logarithmic scale: it is linear in the interval $[-1, 1]$ and logarithmic outside this range, allowing the positive and negative parts and the overall large-scale structure to be displayed in a single plot. The resulting structure is strongly frequency dependent, reflecting the propagation of the intermediate lattice modes.

These results complete the deterministic part of the interaction analysis. The boundary correction modifies the coherent susceptibility through a frequency-dependent self-energy, whose dominant contribution originates from long-wavelength modes. The same structure will play an important role in the noise problem, because thermal fluctuations can also enter the coherent readout channel through these interaction-induced mode-mixing processes. We will turn to this question in the next section.

V. NOISE ANALYSIS OF THE LATTICE

In this section, we analyze the noise properties of the ferromagnet lattice. Under collective readout, different noise sources scale differently with the number of ferromagnets N , depending on whether they are independent at each site or correlated across the lattice. The central advantage of the lattice architecture is that thermal and imprecision-related contributions can be parametrically reduced by collective operation, while backaction can be

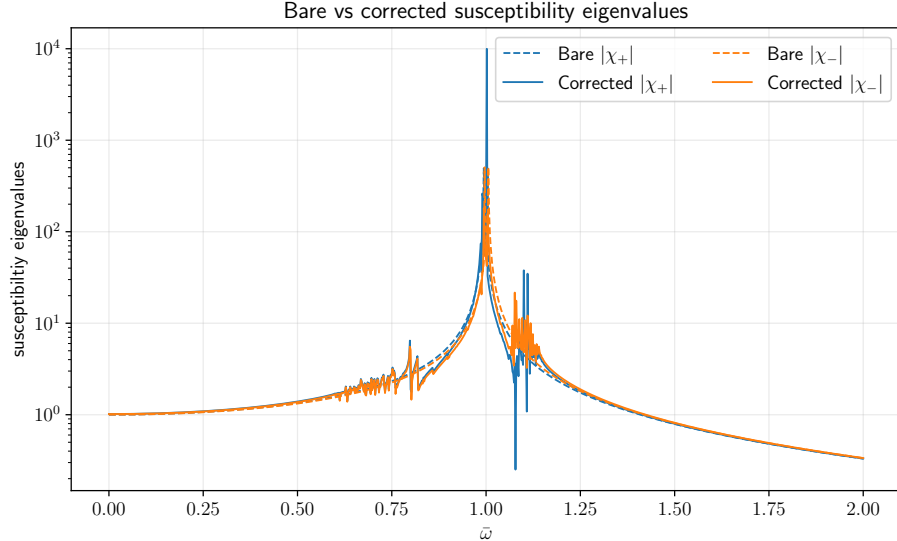


FIG. 4. Comparison between the bare coherent susceptibility and the susceptibility corrected by the boundary-induced self-energy. The finite-size interaction does not simply suppress the response uniformly, but reshapes its spectral structure through enhanced mixing with long-wavelength nonuniform modes, especially near the frequencies associated with the near-singular sector.

rebalanced through the readout circuit. The simple noninteracting scaling must be refined once interaction-induced mode mixing is included. Taking all these effects into account, we show that an effective magnetic-field sensitivity scaling that follows a power law of $1/\sqrt{N}$ can be achieved.

A. Single-ferromagnet noise budget

We begin by reviewing the noise properties of a single levitated ferromagnet, which forms the basis for the lattice analysis. A detailed discussion of the single ferromagnet noise budget can be found in ref. [10, 24]. A weak oscillatory magnetic field induces an angular response of the ferromagnet according to Eq. (10). The angular motion of the ferromagnet produces a magnetic flux signal in the pickup coil, which further produces an induced current as a detection signal. For small angular deviations, the flux can be written as

$$\Phi(\omega) = -\mathbf{x}^T \boldsymbol{\eta} \hat{\mathbf{n}}(\omega), \quad (73)$$

where η is the flux coupling factor between the ferromagnet and the pickup coil, and \mathbf{x} is the coil's normal vector. Assuming that the ferromagnet sits at the center of the coil and that one of its angular directions θ, ϕ is aligned with the coil normal, the flux coupling factor can be derived from direct electromagnetism calculation as

$$\eta = \frac{N_p \mu_0 |\mu|}{2R_p}, \quad (74)$$

where N_p is the number of loops and R_p is the radius of the coil. More generally, for an arbitrary coil geometry, the coupling is described by a matrix that mixes the two angular directions. For simplicity, we restrict attention to symmetrized setups in which the two angular directions are read out independently. Combining Eqs. (10) and (73), the transfer function from magnetic field to measured flux is

$$\mathcal{T}(\omega) \equiv \frac{\Phi(\omega)}{B(\omega)} = \eta \mu \mathbf{x}^\top \chi(\omega) \mathbf{b}. \quad (75)$$

Noise in the measured magnetic field can be traced back to fluctuations in either the mechanical dynamics of the ferromagnet or the readout circuitry. The magnetic field noise spectral density $S_B(\omega)$ is defined by

$$S_B(\omega) = \frac{S_\Phi(\omega)}{|\mathcal{T}(\omega)|^2}, \quad (76)$$

where $S_\Phi(\omega)$ denotes the magnetic flux noise spectrum of the measurement. Specifically, in the fully trapped regime, the susceptibility matrix is diagonal, and in a trivial setup, we align the coils onto the two angular directions θ, ϕ , making the transfer function to be diagonal as well. The system thus introduces no correlation between the two angular directions, as long as the noise spectrum of the readout coils is diagonal itself. We utilize this assumption in the following discussions, as it is generally possible to approximate this condition.

The noise budget receives contributions from three principal physical mechanisms. The first is thermal noise arising from environmental dissipation of the rotational motion. The coupling of the ferromagnet to its surrounding atmosphere introduces a damping rate γ , which, according to the fluctuation-dissipation theorem, is accompanied by a random torque with spectral density

$$S_{\tau,1}^{\text{th}} = 4k_B T I \gamma. \quad (77)$$

Here and in the following, we use the subscript 1 to denote that the term represents a single ferromagnet noise explicitly. This stochastic torque drives angular fluctuations in a similar

way that a magnetic-field-induced torque drives angular motions. The thermal noise can thus be expressed as an equivalent magnetic field noise, which reads

$$S_{B,1}^{\text{th}}(\omega) = \frac{1}{|\mu|^2} S_{\tau,1}^{\text{th}}. \quad (78)$$

In this simplified description, the thermal torque noise is white, and the corresponding equivalent magnetic-field noise is therefore frequency independent.

The second contribution arises from the readout imprecision noise. The SQUID detector possesses an intrinsic flux noise floor characterized by a spectral density $S_{\Phi,1}^{\text{imp}}$. Since this noise enters directly at the readout stage and is independent of the ferromagnet dynamics, the corresponding equivalent magnetic-field noise follows straightforwardly from Eq. (76). Because the transfer function depends on the magnetic susceptibility, the imprecision noise acquires a strong frequency dependence. In particular, it exhibits a pronounced dip at the resonance frequency and increases at large frequencies. At sufficiently high frequencies, the susceptibility approaches zero, causing the imprecision noise to dominate the total noise budget and effectively setting an upper frequency limit for the ferromagnet-based sensor.

The third contribution is the measurement backaction. Fluctuations of the SQUID current generate a fluctuating magnetic field in the pickup circuit, which acts back on the ferromagnet and drives additional motion. Denoting the SQUID current noise by S_I^{SQUID} , the resulting magnetic field noise can be written as

$$S_{B,1}^{\text{back}} = \frac{\eta^2}{|\mu|^2} S_I^{\text{SQUID}}. \quad (79)$$

In contrast to imprecision noise, backaction represents a real fluctuating force acting on the system rather than a limitation of the measurement resolution. The backaction noise is therefore also independent of ferromagnet dynamics or susceptibility matrix, and its spectral form depends solely on S_I^{SQUID} .

The imprecision and backaction noise discussed above originate from the same physical source, namely the intrinsic quantum fluctuations of the SQUID detector. In the readout process, the SQUID converts the magnetic flux induced by the ferromagnet into a measurable output signal, while its current fluctuations are fed back into the pickup circuit and generate a fluctuating magnetic field acting on the ferromagnet. These two effects define the two complementary noise channels of the readout: the flux imprecision noise S_{Φ}^{imp} and the SQUID current noise S_I^{SQUID} . For a linear quantum detector, these two noise channels are not

independent. Following Ref. [10], it is convenient to characterize them by the two energy-resolution parameters

$$\kappa_\Phi \equiv \frac{S_\Phi^{\text{imp}}}{L_S}, \quad \kappa_I \equiv S_I^{\text{SQUID}} L_S, \quad (80)$$

where L_S is the SQUID inductance. The quantum limit constrains their product as $\kappa_\Phi \kappa_I \gtrsim \hbar^2$, up to convention-dependent factors of order unity [10, 25]. In the present work, we follow Ref. [10] and adopt the symmetric choice

$$\kappa_\Phi = \kappa_I = \kappa, \quad (81)$$

so that the flux and current noise are taken to contribute equally in the sense of energy resolution. Under this assumption,

$$S_\Phi^{\text{imp}} = L_S \kappa, \quad S_I^{\text{SQUID}} = \frac{\kappa}{L_S}, \quad \frac{S_\Phi^{\text{imp}}}{S_I^{\text{SQUID}}} = L_S^2. \quad (82)$$

For the numerical estimates, we take $\kappa = 1000 \hbar$ for the current setup following Ref. [10].

Combining the three contributions, the total magnetic field noise spectrum of a single levitated ferromagnet can be written as

$$S_{B,1}(\omega) = S_{B,1}^{\text{th}}(\omega) + S_{B,1}^{\text{imp}}(\omega) + S_{B,1}^{\text{back}}(\omega). \quad (83)$$

This single-particle noise budget provides the reference against which the noise properties of the ferromagnet lattice will be evaluated in the following sections.

B. Collective readout, interaction correction, and noise scaling

We now extend the single-particle noise analysis to the lattice. In the ideal collective-readout picture, the total signal is obtained by coherently summing the responses of all ferromagnets, while different noise sources scale differently depending on whether they are correlated across the lattice. However, once the dipole-dipole interaction and the finite boundary are taken into account, this simple scaling picture must be refined. As shown in Sec. IV, the finite boundary mixes the coherent mode with nonuniform modes, and the resulting correction affects different noise channels in qualitatively different ways.

The key distinction is whether the noise source acts directly on the coherent channel alone or drives all lattice modes. A spatially uniform external signal couples only to the coherent mode and acquires an interaction correction only through virtual leakage into nonuniform

modes and back, as encoded in the boundary self-energy. Thermal noise behaves differently: since it acts independently on each ferromagnet, it excites all reciprocal-space modes directly. The thermal fluctuations of nonuniform modes can therefore enter the coherent readout channel through boundary-induced mode mixing. This mechanism leads to an additional interaction-dependent correction to the thermal noise, which is absent in the noninteracting picture. By contrast, as will be discussed below, the imprecision and backaction noise remain tied primarily to the coherent readout channel and do not acquire this extra mixing-induced contribution.

1. Thermal noise

We begin with thermal noise. For a single ferromagnet, the thermal torque noise can be represented as an equivalent white magnetic-field noise with spectral density

$$S_{B,1}^{\text{th}}(\omega) = \frac{4k_B T I \gamma}{|\mu|^2} \mathbb{1}, \quad (84)$$

where the noise is assumed to be identical and uncorrelated in the two orthogonal angular directions. In the lattice, thermal noise acts independently on each ferromagnet and can therefore be modeled as a random local magnetic field $\mathbf{B}_i^{\text{noise}}(\omega)$. The equation of motion in the reciprocal space reads

$$\chi_{\text{mod}}^{-1}(\omega, \mathbf{k}) \mathbf{u}_{\mathbf{k}}(\omega) - \mu B_{\text{dd}} \sum_{\mathbf{q} \neq \mathbf{k}} V_{\mathbf{kq}} \mathbf{u}_{\mathbf{q}}(\omega) = -\mu [\mathbf{B}_{\text{ext}}(\omega) \delta_{\mathbf{k},0} + \mathbf{B}^{\text{noise}}(\omega, \mathbf{k})]. \quad (85)$$

The thermal noise in real space is uncorrelated between different ferromagnets,

$$\langle \mathbf{B}_i^{\text{noise}}(\omega) \mathbf{B}_j^{\text{noise}}(\omega')^\dagger \rangle = 2\pi \delta(\omega - \omega') \delta_{ij} S_{B,1}^{\text{th}}, \quad (86)$$

and therefore remains uncorrelated between different \mathbf{k} modes after Fourier transformation,

$$\langle \mathbf{B}^{\text{noise}}(\omega, \mathbf{k}) \mathbf{B}^{\text{noise}}(\omega', \mathbf{k}')^\dagger \rangle = \frac{2\pi}{N} \delta(\omega - \omega') \delta_{\mathbf{k}\mathbf{k}'} S_{B,1}^{\text{th}}. \quad (87)$$

Thus, thermal noise is white both in real space and in reciprocal space, but unlike an external signal it acts on all lattice modes rather than only on the coherent mode. This is the essential difference between thermal noise and a spatially uniform external field. The external field enters only through the $\mathbf{k} = 0$ channel, and its interaction correction arises because the coherent response leaks into nonuniform modes and then returns. Thermal noise, however,

directly drives every \mathbf{k} mode. As a result, the thermal fluctuations of nonuniform modes can contribute to the coherent readout through the same boundary-induced mode mixing discussed in Sec. IV. In the coherent-mode-dominance regime, the equations of motion take the form

$$\chi_{\text{mod}}^{-1}(\omega, \mathbf{k})\mathbf{u}_{\mathbf{k}} - \mu B_{\text{dd}} V_{\mathbf{k}0}\mathbf{u}_0 = -\mu \mathbf{B}^{\text{noise}}(\omega, \mathbf{k}), \quad \mathbf{k} \neq 0, \quad (88)$$

and

$$\chi_{\text{mod}}^{-1}(\omega, \mathbf{0})\mathbf{u}_0 - \mu B_{\text{dd}} \sum_{\mathbf{k} \neq 0} V_{0\mathbf{k}}\mathbf{u}_{\mathbf{k}} = -\mu [\mathbf{B}_{\text{ext}}(\omega) + \mathbf{B}^{\text{noise}}(\omega, 0)]. \quad (89)$$

Solving these equations to leading order gives

$$\mathbf{u}_0 = -\mu \chi_{\text{coh}}(\omega) [\mathbf{B}_{\text{ext}}(\omega) + \mathbf{B}_{\text{eff}}^{\text{noise}}(\omega)], \quad (90)$$

where

$$\mathbf{B}_{\text{eff}}^{\text{noise}}(\omega) = \mathbf{B}^{\text{noise}}(\omega, 0) + \mu B_{\text{dd}} \sum_{\mathbf{k} \neq 0} V_{0\mathbf{k}} \chi_{\text{mod}}(\omega, \mathbf{k}) \mathbf{B}^{\text{noise}}(\omega, \mathbf{k}). \quad (91)$$

is the effective thermal magnetic field acting on the coherent mode. Compared with the response to an external signal, there is an additional contribution from the thermal noise of all nonuniform modes. The first term in $\mathbf{B}_{\text{eff}}^{\text{noise}}(\omega)$ is the direct coherent contribution, which would remain in the noninteracting limit. The second term is induced entirely by the interaction and the finite boundary, and describes the conversion of thermal fluctuations from nonuniform modes into the coherent readout channel.

Using Eq. (87), the correlation function of the effective thermal field becomes

$$\begin{aligned} & \langle \mathbf{B}_{\text{eff}}^{\text{noise}}(\omega) \mathbf{B}_{\text{eff}}^{\text{noise}}(\omega')^\dagger \rangle \\ &= \frac{2\pi}{N} \delta(\omega - \omega') \left[\mathbb{1} + |\mu|^2 B_{\text{dd}}^2 \sum_{\mathbf{k} \neq 0} V_{0\mathbf{k}} \chi_{\text{mod}}(\omega, \mathbf{k}) \chi_{\text{mod}}^\dagger(\omega, \mathbf{k}) V_{\mathbf{k}0} \right] S_{B,1}^{\text{th}}. \end{aligned} \quad (92)$$

The equivalent thermal magnetic-field noise of the lattice is therefore

$$S_B^{\text{th}}(\omega) = \frac{1}{N} M S_{B,1}^{\text{th}}, \quad (93)$$

where

$$M = \mathbb{1} + |\mu|^2 B_{\text{dd}}^2 \sum_{\mathbf{k} \neq 0} V_{0\mathbf{k}} \chi_{\text{mod}}(\omega, \mathbf{k}) \chi_{\text{mod}}^\dagger(\omega, \mathbf{k}) V_{\mathbf{k}0} \quad (94)$$

is a 2×2 matrix that rescales the thermal noise. Rewriting this in terms of the dimensionless susceptibility defined in Sec. IV yields

$$M = \mathbb{1} + \lambda_{\text{int}}^2 \sum_{\mathbf{k} \neq 0} V_{0\mathbf{k}} \xi^{-1}(\omega, \mathbf{k}) \xi^{-1}(\omega, \mathbf{k})^\dagger V_{\mathbf{k}0}. \quad (95)$$

This result should be contrasted with the deterministic boundary self-energy in Sec. IV.B. The self-energy depends linearly on the susceptibility of the intermediate modes, whereas the thermal-noise correction depends quadratically on it. Thermal noise is therefore more sensitive to near-singular modes than the coherent susceptibility itself. Even when the deterministic response is only moderately distorted, the thermal noise can already be strongly amplified once the lattice contains modes with anomalously large susceptibility.

When the near-singular modes must be retained explicitly, the same logic applies, except that the susceptibility of an isolated mode is replaced by the full response matrix of the near-singular subspace. The thermal noise then becomes

$$S_B^{\text{th}}(\omega) = \frac{1}{N} \left[\mathbb{1} + \lambda_{\text{int}}^2 \sum_{\mathbf{s}_1, \mathbf{s}_2, \mathbf{s}_3 \in \mathcal{S} \setminus \{0\}} V_{0\mathbf{s}_1} G_{\mathbf{s}_1, \mathbf{s}_2}(\omega) G_{\mathbf{s}_2, \mathbf{s}_3}^\dagger(\omega) V_{\mathbf{s}_3 0} \right] S_{B,1}^{\text{th}}. \quad (96)$$

Thus, the perturbative and nonperturbative treatments have the same formal structure as in Sec. IV: the near-singular modes are simply promoted from isolated intermediate responses to a coupled response matrix.

Numerical results for the thermal-noise matrix are shown in FIG. 5. Because the correction depends on the square of the susceptibility, the thermal noise is drastically amplified in the frequency range where near-singular modes appear. The interaction therefore creates a blind zone in the frequency band, within which the final sensitivity is strongly degraded even though the coherent susceptibility itself is not parametrically suppressed. In the small- \mathbf{k} approximation, the boundaries of this blind zone are given by Eq.(65). The exact numerical result is slightly broader than this small- \mathbf{k} estimate, while still remaining in good overall agreement with it. We also note that, within parts of the blind zone, the thermal-noise matrix develops nonzero off-diagonal components, indicating interaction-induced correlations between the two orthogonal angular directions.

The thermal-noise result above constitutes the main modification of the ideal collective-readout picture. In the absence of interaction, thermal noise is reduced simply by averaging over independent ferromagnets, achieving a suppression factor of $1/N$. In the interacting finite lattice, however, this $1/N$ scaling is supplemented by a frequency-dependent correction arising from the conversion of nonuniform thermal fluctuations into coherent readout noise. Nevertheless, this blind zone is concentrated only around a small region about the resonance frequency, and for most of the remaining frequency range the thermal noise still remains the favorable $1/N$ scaling. This blind zone can be further compensated for by adopting two

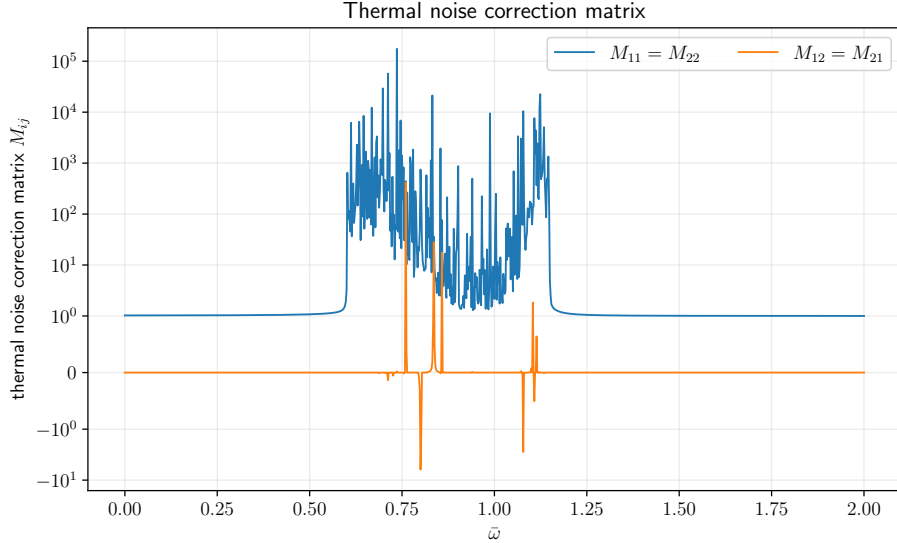


FIG. 5. Components of the thermal magnetic-field noise matrix for the finite simple cubic lattice. The vertical axis is shown on a symmetric logarithmic scale that is linear in the interval $[-1, 1]$ and logarithmic outside this range. The interaction-induced correction strongly amplifies the thermal noise in the frequency range where near-singular modes appear. As a result, the lattice develops a blind zone in which the observable sensitivity is significantly degraded. The off-diagonal components become nonzero within part of this region, showing that the boundary-induced mode mixing also generates correlations between the two orthogonal angular directions.

distinct resonance frequencies in two experiments, to which we will return in the numerical part.

2. Imprecision and backaction noise

We next consider the readout-induced noise channels, which predominantly comprise imprecision and backaction noise. Unlike thermal noise, these contributions do not originate from independent fluctuations acting on each ferromagnet. Instead, they are tied directly to the collective readout process itself, and therefore couple primarily to the coherent channel. As a result, they do not acquire an additional boundary-induced correction of the thermal-noise type.

The imprecision noise originates from the intrinsic flux noise floor of the SQUID detector. Since this noise enters directly at the readout stage, its equivalent magnetic-field noise is

determined by the inverse transfer function from the external magnetic field to the measured collective flux. In the interacting finite lattice, the only modification is therefore that the single-particle susceptibility appearing in the transfer function must be replaced by the corrected coherent susceptibility derived above. For a collective readout aligned with the coherent channel, the total flux can be written as

$$\Phi_{\text{tot}}(\omega) = N \eta \mu \mathbf{x}^T \chi_{\text{coh}}(\omega) \mathbf{b} B(\omega), \quad (97)$$

so that the collective transfer function becomes

$$\mathcal{T}_{\text{coh}}(\omega) = N \eta \mu \mathbf{x}^T \chi_{\text{coh}}(\omega) \mathbf{b}. \quad (98)$$

The corresponding imprecision noise is therefore

$$S_B^{\text{imp}}(\omega) = \frac{S_{\Phi}^{\text{imp}}(\omega)}{|\mathcal{T}_{\text{coh}}(\omega)|^2}. \quad (99)$$

Compared with the ideal noninteracting lattice, no additional contribution from nonuniform modes appears in the numerator. The effect of the interaction is entirely contained in the corrected coherent response entering $\mathcal{T}_{\text{coh}}(\omega)$.

This point is physically important. The imprecision noise is not a fluctuating force acting on the lattice degrees of freedom, but a limitation of how accurately the collective flux can be read out. It therefore does not excite nonuniform lattice modes independently, and there is no analog of Eq. (91) for the imprecision channel. In the limit where the coherent response reduces to the ideal collective sum, Eq. (99) recovers a $1/N^2$ suppression.

The backaction noise behaves in a different manner. It originates from current fluctuations in the SQUID readout circuit, which generate a fluctuating magnetic field in the pickup coil. Because this magnetic field is produced collectively by the readout circuit and is approximately uniform across the lattice, it couples predominantly to the coherent mode. Its role is therefore analogous to that of an external spatially uniform driving field, except that the field is stochastic rather than deterministic. Consequently, the backaction noise does not receive an extra contribution from independently fluctuating nonuniform modes, and its equivalent magnetic-field spectrum is still determined directly by the readout circuit,

$$S_B^{\text{back}}(\omega) = \frac{\eta^2}{|\mu|^2} S_I^{\text{SQUID}}(\omega). \quad (100)$$

As the backaction magnetic field is correlated across all the ferromagnets, there is no additional suppression due to the number of ferromagnets N .

The contrast with thermal noise is therefore clear. Thermal fluctuations act locally on each ferromagnet, and after transforming to reciprocal space they appear as independent noise sources for all \mathbf{k} modes. This is why boundary-induced mode mixing generates the additional correction in Eqs. (93)-(96), leading to a blind zone. The imprecision and backaction noise, by contrast, are both associated with the collective readout channel itself. The former enters directly as detector noise in the measured flux, and the latter enters as an approximately uniform stochastic magnetic field generated by the pickup circuit. Neither of them produces an additional incoherent injection into nonuniform lattice modes analogous to the thermal-noise channel.

Collecting the above results, the total magnetic-field noise of the lattice can be written schematically as

$$S_B(\omega) = S_B^{\text{th}}(\omega) + S_B^{\text{imp}}(\omega) + S_B^{\text{back}}(\omega), \quad (101)$$

where the thermal contribution is given by the interaction-corrected expressions in Eqs. (93) and (96), the imprecision noise is obtained from the corrected coherent transfer function through Eq. (99), and the backaction noise remains determined by the collective pickup-circuit fluctuations through Eq. (100). In the ideal limit away from the near-singular band, these expressions reduce to the familiar scaling relations

$$S_B^{\text{th}} \sim \frac{1}{N}, \quad S_B^{\text{imp}} \sim \frac{1}{N^2}, \quad S_B^{\text{back}} \sim N^0. \quad (102)$$

The main new feature of the interacting finite lattice is therefore not a qualitative change in the imprecision or backaction channels, but the strong interaction-induced amplification of the thermal noise near the near-singular sector.

3. *Readout rebalancing and optimization of the effective coupling*

According to the previous result, the three noise components scale differently. Thermal fluctuations are suppressed through averaging over independent particles, imprecision noise benefits from the enhanced collective signal, while backaction noise remains correlated across the lattice and therefore sets an important limit that must be mitigated through readout optimization. The relative magnitude of the imprecision and backaction contributions depends on the coupling between the pickup coil and the SQUID readout circuit. This coupling is characterized by the flux coupling factor η introduced in Eq. (73), which determines both

the strength of the signal readout and the magnitude of the current fluctuations fed back to the ferromagnet. As a result, the imprecision and backaction noise contributions exhibit opposite dependences on η . Increasing the coupling improves the transfer of magnetic flux to the SQUID and therefore reduces the equivalent magnetic field imprecision noise, while at the same time amplifying the magnetic field fluctuations generated by SQUID current noise.

This trade-off can be understood directly from the expressions for the noise contributions. The imprecision noise is obtained by dividing the intrinsic SQUID flux noise by the square of the transfer function defined in Eq. (75). Since the transfer function is proportional to the coupling factor η , the equivalent magnetic field noise scales as

$$S_B^{\text{imp}}(\omega) \propto \eta^{-2}. \quad (103)$$

In contrast, the backaction noise originates from SQUID current fluctuations that produce a magnetic field through the pickup circuit. The magnitude of this field is proportional to the same coupling factor, leading to

$$S_B^{\text{back}}(\omega) \propto \eta^2. \quad (104)$$

The two contributions therefore vary in opposite directions as the coupling strength is adjusted. Because the imprecision and backaction noise originate from the same quantum fluctuations of the SQUID detector, their spectral densities cannot be reduced simultaneously. The uncertainty relation discussed in Sec. V.A implies that decreasing the flux noise necessarily increases the associated current fluctuations.

In practice, this balancing can be implemented by introducing a two-stage pickup circuit. One pickup coil with inductance L_p couples directly to the ferromagnet lattice, while a second coil with inductance L_i is coupled to the SQUID input coil of inductance L_s . The two pickup coils are connected in series and therefore carry the same current. If the mutual inductance between the intermediate coil and the SQUID input coil is $M_i = k\sqrt{L_i L_s}$, with $k < 1$ determined by the circuit geometry, the entire readout chain is equivalent to a single effective coupling in which the flux coupling η is rescaled by a factor M_i/L_{tot} , where $L_{\text{tot}} = L_p + L_i$. Accordingly, the effective transfer function acquires the replacement

$$\eta \rightarrow \eta_{\text{eff}} \equiv \eta \frac{M_i}{L_{\text{tot}}}. \quad (105)$$

Since the backaction noise is generated by SQUID current fluctuations fed back through the same circuit, it scales as η_{eff}^2 , whereas the imprecision noise, obtained by dividing the SQUID flux noise by the square of the transfer function, scales as η_{eff}^{-2} . The readout optimization problem therefore reduces to choosing the circuit parameters such that η_{eff} places the two contributions at comparable levels in the frequency range of interest.

For a circular pickup coil of radius R_p and loop number N_p , the coil inductance is

$$L_p = N_p^2 \mu_0 R_p \left[\ln \left(\frac{8R_p}{a_p} \right) - 2 \right], \quad (106)$$

with a_p the wire radius. Varying N_p or R_p therefore changes both the direct magnetic coupling and the total inductance of the pickup circuit, and hence provides a practical way to tune η_{eff} . This tuning plays qualitatively different roles in the single-ferromagnet and lattice cases. For a single ferromagnet, one generally seeks to maximize η_{eff} until the backaction and imprecision contributions become comparable, since stronger coupling directly improves the readout. For a lattice, however, the imprecision contribution is already suppressed by the collective factor $1/N^2$, so the optimal strategy is typically to reduce η_{eff} relative to the single-particle optimum in order to lower the correlated backaction noise without sacrificing the overall sensitivity. Parametrically, their relative magnitude scales as

$$\frac{S_B^{\text{back}}(\omega = 0)}{S_B^{\text{imp}}(\omega = 0)} = \frac{N^2 \eta_{\text{eff}}^4 S_I^{\text{SQUID}}(\omega = 0)}{V_{\theta\theta}^2 S_{\Phi}^{\text{imp}}(\omega = 0)}, \quad (107)$$

where $V_{\theta\theta}$ denotes the relevant curvature of the trapping potential. The optimal readout configuration is therefore achieved when the quantity in Eq. (107) is of order unity whenever possible, or otherwise minimized if the backaction contribution remains dominant throughout the accessible parameter range. In this way, the correlated backaction noise can be rebalanced down to the level of the thermally limited floor, while retaining the strong collective suppression of the imprecision noise.

C. Secondary imperfections of the lattice

The analysis above identifies the dominant interaction-induced modification of the lattice noise: the finite boundary mixes the coherent mode with nonuniform modes, and this mixing strongly amplifies the thermal noise in the near-singular band. In the discussions before, we assumed an ideal lattice model with identical ferromagnets and an exact scale hierarchy.

In a realistic implementation, however, the lattice is not perfectly ideal. Small fabrication-induced variations among the ferromagnets and the finite spatial extent of the readout geometry introduce additional corrections beyond the ideal lattice model. These effects do not change the basic physical mechanism responsible for the blind zone, but they can modify the detailed structure of the response and the noise spectrum.

In the following, we discuss two such secondary imperfections. The first is fabrication-induced disorder in the local single-particle response, which enters the mode-space dynamics as an additional kernel on top of the boundary correction. The second is the spatial nonuniformity of the readout and backaction profiles, which causes the measured signal and the backaction drive to deviate slightly from a pure projection onto the coherent channel. Both effects can be incorporated naturally into the reciprocal-space framework developed above. Their main impact is to reshape the detailed structure of the response within the blind zone, while leaving the behavior outside that region only weakly affected.

1. Fabrication-induced disorder in the dynamical kernel

We first consider fabrication-induced variations among the ferromagnets. In an ideal lattice, all particles are assumed to have identical properties, so that the single-particle susceptibility is the same on every site. In practice, however, small variations in radius, magnetic moment, moment of inertia, trap curvature, or equilibrium orientation lead to a weak site dependence of the local response. This can be described by writing the single-particle inverse susceptibility on site i as

$$\chi_i^{-1}(\omega) = \chi^{-1}(\omega) + \delta K_i(\omega), \quad (108)$$

where $\chi(\omega)$ is the ideal susceptibility and $\delta K_i(\omega)$ denotes the local fabrication-induced deviation. In real space, the lattice equation of motion then becomes

$$\sum_j [\chi^{-1}(\omega)\delta_{ij} + \delta K_i(\omega)\delta_{ij} - \mu B_{\text{dd}}T_{ij}] \delta \mathbf{n}_j(\omega) = -\mu \mathbf{B}_i(\omega), \quad (109)$$

where \mathbf{B}_i denotes the total magnetic field acting on site i .

After transforming to reciprocal space, the disorder term is no longer diagonal in momentum space. Instead, it generates an additional mode-mixing kernel

$$\delta K_{\mathbf{kq}}(\omega) \equiv \frac{1}{N} \sum_i e^{-i\mathbf{k}\cdot\mathbf{r}_i} \delta K_i(\omega) e^{i\mathbf{q}\cdot\mathbf{r}_i}, \quad (110)$$

which enters the mode-space equation on exactly the same footing as the boundary correction. The equation of motion therefore takes the form

$$\chi_{\text{mod}}^{-1}(\omega, \mathbf{k})\mathbf{u}_{\mathbf{k}} - \mu B_{\text{dd}} \sum_{\mathbf{q}} V_{\mathbf{kq}}\mathbf{u}_{\mathbf{q}} + \sum_{\mathbf{q}} \delta K_{\mathbf{kq}}(\omega)\mathbf{u}_{\mathbf{q}} = -\mu \mathbf{B}_{\mathbf{k}}(\omega). \quad (111)$$

Equivalently, one may regard the disorder correction as simply shifting the mode-mixing kernel according to

$$V_{\mathbf{kq}} \rightarrow V_{\mathbf{kq}} - \frac{1}{\mu B_{\text{dd}}} \delta K_{\mathbf{kq}}(\omega). \quad (112)$$

All of the formalism developed in Secs. IV and V.B then remains valid after this replacement. Therefore, the fabrication disorder does not introduce a qualitatively new mechanism, but rather modifies the same leakage processes already induced by the finite boundary. The coherent mode can still couple to nonuniform modes, except that the corresponding mode-mixing amplitudes are now shifted by the additional kernel $\delta K_{\mathbf{kq}}$. As a result, the self-energy correction to the coherent susceptibility and the interaction-induced correction to the thermal noise are both modified in a straightforward way by the replacement in Eq. (112).

A rough estimate of the size of this effect can be obtained by introducing a characteristic relative fabrication error ε_{dis} , representing the typical fractional variation of the microscopic parameters entering the local susceptibility. Since δK_i arises from these local variations, one expects its matrix elements to scale as

$$\|\delta K_i\| \sim \varepsilon_{\text{dis}} \|\chi^{-1}\|, \quad (113)$$

and therefore the corresponding mode-space kernel satisfies

$$\|\delta K_{\mathbf{kq}}\| \sim \varepsilon_{\text{dis}} \|\xi(\omega, \mathbf{k})\|, \quad (114)$$

up to geometric factors associated with the Fourier transform. Away from the near-singular region, where the lattice response remains regular, such corrections remain perturbative and lead only to small quantitative shifts in the response. Inside the blind zone, as the inverse susceptibility is already strongly enhanced, a relatively weak $\delta K_{\mathbf{kq}}$ can reshape the detailed line shape by shifting, broadening, or splitting the structures generated by the near-singular modes. The important point is that fabrication disorder does not by itself create a new broad noise-dominated band. Its main effect is to modify the detailed structure within the interaction-induced blind zone, where the coherent response is already highly sensitive

to mode mixing. Outside that region, the response and noise spectra remain controlled primarily by the ideal kernel and the boundary correction, with disorder contributing only a small perturbative correction. In this sense, the interaction-induced blind zone is robust against moderate fabrication imperfections. Disorder changes its fine structure, but not the basic physical origin of the effect or its overall location in frequency space.

2. *Nonuniform readout and backaction profiles*

A second secondary imperfection arises from the finite spatial extent of the lattice and the nonuniformity of the pickup-circuit field profile. In the ideal discussion above, both the readout and the backaction are assumed to couple purely to the coherent mode. This approximation is exact only when the lattice is much smaller than the spatial variation scale of the pickup coil, so that the readout sensitivity and the backaction field are both effectively uniform across the array. In a finite lattice, however, this is only approximately true: the measured flux is no longer a perfect projection onto the coherent channel, and the stochastic backaction field generated by the pickup circuit is no longer perfectly uniform. Both effects introduce a small admixture of nonuniform modes into the readout channel.

To describe this, let $g(\mathbf{r}_i)$ denote the spatial profile with which the pickup coil samples the motion of the i th ferromagnet. The measured flux can then be written as

$$\Phi(\omega) = \eta \sum_i g(\mathbf{r}_i) \mathbf{x}^\top \delta \mathbf{n}_i(\omega). \quad (115)$$

Transforming to reciprocal space gives

$$\Phi(\omega) = \eta \sum_{\mathbf{k}} g_{-\mathbf{k}} \mathbf{x}^\top \mathbf{u}_{\mathbf{k}}(\omega), \quad (116)$$

where

$$g_{\mathbf{k}} = \sum_i g(\mathbf{r}_i) e^{-i\mathbf{k} \cdot \mathbf{r}_i} \quad (117)$$

is the reciprocal-space readout profile. In the ideal limit of perfectly uniform pickup sensitivity, one has $g(\mathbf{r}_i) = \text{const}$, and therefore

$$g_{\mathbf{k}} \propto \delta_{\mathbf{k},0}. \quad (118)$$

So that the readout projects purely onto the coherent mode. For a finite lattice and a smooth but nonuniform pickup profile, however, the coefficients $g_{\mathbf{k} \neq 0}$ become small but nonzero, and the measured signal acquires a weak contribution from nonuniform modes.

The same logic applies to the backaction channel. Let $f(\mathbf{r}_i)$ denote the spatial profile of the stochastic magnetic field generated by the pickup circuit and acting back on the lattice. In real space, the backaction drive on site i may be written as

$$\mathbf{B}_i^{\text{back}}(\omega) = f(\mathbf{r}_i) \mathbf{B}^{\text{back}}(\omega), \quad (119)$$

where $\mathbf{B}^{\text{back}}(\omega)$ is the stochastic backaction field amplitude. In reciprocal space this becomes

$$\mathbf{B}_{\mathbf{k}}^{\text{back}}(\omega) = f_{\mathbf{k}} \mathbf{B}^{\text{back}}(\omega), \quad (120)$$

with

$$f_{\mathbf{k}} = \sum_i f(\mathbf{r}_i) e^{-i\mathbf{k}\cdot\mathbf{r}_i}. \quad (121)$$

In the ideal uniform-field limit, $f_{\mathbf{k}} \propto \delta_{\mathbf{k},0}$ and the backaction drives only the coherent mode. In a realistic finite geometry, the coefficients $f_{\mathbf{k}\neq 0}$ are again small but nonzero, so that the backaction field also acquires a weak coupling to nonuniform modes.

These two effects are closely analogous. The readout profile determines which linear combination of lattice modes is observed, while the backaction profile determines which linear combination of lattice modes is driven by the stochastic field of the pickup circuit. Both reduce to the coherent channel in the uniform limit, and both acquire small nonuniform admixtures when the spatial profile varies across the lattice.

The magnitude of this correction may be estimated directly from the smoothness of the profile functions. If the characteristic lattice size is L_{lat} and the pickup-coil has radius R_p , then for a lattice centered on the symmetry axis one expects the first nonvanishing correction to arise at quadratic order in position. Expanding a smooth profile around the lattice center gives

$$g(\mathbf{r}) = g_0 + \frac{1}{2} G_{ab} r^a r^b + \mathcal{O}(r^3), \quad (122)$$

and similarly

$$f(\mathbf{r}) = f_0 + \frac{1}{2} F_{ab} r^a r^b + \mathcal{O}(r^3), \quad (123)$$

where the linear terms vanish for a lattice centered at a symmetry point. The relative magnitude of the nonuniform part is therefore parametrically

$$\frac{g_{\mathbf{k}\neq 0}}{g_0} \sim \frac{f_{\mathbf{k}\neq 0}}{f_0} \sim O\left(\frac{L_{\text{lat}}^2}{R_p^2}\right), \quad (124)$$

up to geometry-dependent coefficients.

Within the reciprocal-space formalism, the effect of these profiles is straightforward. The coherent transfer function is replaced by the more general readout projection in Eq. (116), and the backaction drive is no longer proportional solely to $\delta_{\mathbf{k},0}$ but instead to the profile $f_{\mathbf{k}}$. Thus, the observable signal and the backaction noise both receive small corrections from nonuniform modes. These corrections are again most relevant in the near-singular region, where the amplitude of the nonuniform sector is already strongly enhanced. Outside the blind zone, however, the response of nonuniform modes remains regular and the contributions from $g_{\mathbf{k}\neq 0}$ and $f_{\mathbf{k}\neq 0}$ remain perturbatively small.

The physical consequence is therefore similar to that of fabrication disorder, although its origin is different. A nonuniform readout or backaction profile does not create a new dominant noise mechanism. Instead, it modifies the detailed way in which the lattice is observed and driven, and hence slightly reshapes the fine structure of the response and noise near the blind zone. Away from that region, the readout and backaction remain well approximated by pure coherent-channel coupling. A direct implication is that a pickup-coil geometry with a controlled admixture of noncoherent modes in the readout is in fact acceptable, and can even be advantageous from the perspective of the overall noise budget. This point is particularly important for maximizing the signal extraction from the lattice. If the pickup coil is taken to be excessively large compared with the lattice, the magnetic coupling between the coil and the ferromagnets becomes weak, which directly enlarges the equivalent imprecision-noise contribution. By contrast, a coil whose size is closer to that of the lattice can achieve substantially stronger coupling to the ferromagnets, thereby reducing the total noise floor, even though the corresponding readout channel is no longer a perfectly pure projection onto the coherent mode. In this sense, a small admixture of noncoherent modes should be viewed as an acceptable tradeoff, rather than as a fundamental obstacle, whenever the improvement in the effective coupling is sufficient to compensate for the resulting mode impurity. To minimize the adverse impact of such noncoherent-mode admixture, one should in particular avoid mechanical noise sources whose spatial structure is resonant with the lattice scale, since these modes can be preferentially transduced once the readout departs from a purely coherent projection.

We have performed numerical calculations for a simple circular-coil geometry whose center is aligned with that of the lattice. The results show that when the coil radius is chosen to be five times the lattice side length, the coupling of noncoherent modes to the coil is only about

10^{-3} of that of the coherent mode. If the coil radius is instead reduced to be comparable to the lattice side length, so that the lattice nearly fills the interior of the coil, the coupling to noncoherent modes increases to about 0.1 of the coherent-mode coupling. At the same time, however, the effective coupling coefficient η_{eff} is enhanced by several tens of times. For the present geometry, where the total noise is primarily dominated by imprecision noise, this tradeoff is favorable, since the gain in signal transduction more than compensates for the moderate loss of coherent-mode purity. In other parameter regimes, where imprecision noise is no longer dominant or can be efficiently balanced against backaction noise, it may instead be preferable to adopt a somewhat larger coil radius, thereby obtaining a readout channel closer to a pure coherent-mode projection.

Taken together, the two secondary imperfections discussed in this subsection have a common effect: they perturb the ideal coherent-channel picture without changing its basic validity over most of the spectrum. Fabrication disorder modifies the dynamical kernel itself, while finite-profile readout and backaction introduce small nonuniform projections in the measurement and drive channels. Both effects are strongly amplified only in the same near-singular frequency range already identified in the ideal analysis. They therefore alter the detailed internal structure of the blind zone, but not the existence of the blind zone or the overall behavior away from it.

D. Benchmark parameters and numerical noise spectra

Having established the general noise budget of the lattice magnetometer, we now specify a representative set of benchmark parameters and evaluate the corresponding noise spectra. The goal of this subsection is not to perform a complete global optimization over all possible experimental configurations. Instead, we first identify the dominant scaling relations that govern the parameter dependence, and then choose a concrete benchmark configuration that keeps the interaction-induced mode mixing under control while maintaining a realistic macroscopic lattice size.

The most important constraint comes from the interaction parameter λ_{int} . This parameter characterizes the strength of the residual dipole-dipole interaction relative to the trapping curvature, and must remain sufficiently small for the perturbative treatment of the interaction-induced mode mixing to remain valid. For fixed λ_{int} , the trapping curvature is

TABLE I. Benchmark parameters of the ferromagnet lattice and readout apparatus used in the numerical calculations. Parameters marked with an asterisk are directly adopted from ref. [10], including the microscopic properties of each individual ferromagnet, the thermal environment, and the SQUID-related quantities. The remaining parameters are introduced or estimated in the present work in order to describe the lattice geometry, the trapping configuration, and the collective readout circuit.

Parameters	Values
*Ferromagnet radius R	20 μm
*Ferromagnet magnetization M	7.0×10^5 A/m
*Ferromagnet dipole μ	-2.3×10^{-8} A \cdot m ²
*Ferromagnet density ρ	7400 kg/m ³
*Einstein de-Haas frequency ω_1	3.3 Hz
*Magnetization frequency scale ω_s (Neodymium magnet)	1.5×10^{11} Hz
*Temperature T	4.0 K
*Dissipation rate γ	10^{-2} Hz
*Energy resolution κ	$1000\hbar$
Trapping potential $V_{\theta\theta} = V_{\phi\phi}$	10^{-13} J
Ferromagnet number N	10^6
Lattice constant a_0	2000 μm
Pickup coil radius R_p	200 mm
*Pickup coil wire radius a_p	0.1 mm
*SQUID inductance L_s	80 pH
*Intermediate coil inductance L_i	1.8 μH
Coupling coefficient $\eta/\sqrt{L_s}$ (without rescaling)	8.0×10^{-9} $\sqrt{\text{J}}$
Rescaled coupling coefficient $\eta_{\text{eff}}/\sqrt{L_s}$	2.2×10^{-11} $\sqrt{\text{J}}$

constrained by

$$V_{\theta\theta} = \frac{\omega_s}{\gamma_e \lambda_{\text{int}}} \frac{R^3}{a_0^3} \mu \propto R^6 a_0^{-3}, \quad (125)$$

where R is the radius of each ferromagnet and a_0 is the lattice constant. Therefore, once the single-particle design and the target value of λ_{int} are fixed, a_0 and $V_{\theta\theta}$ can no longer be

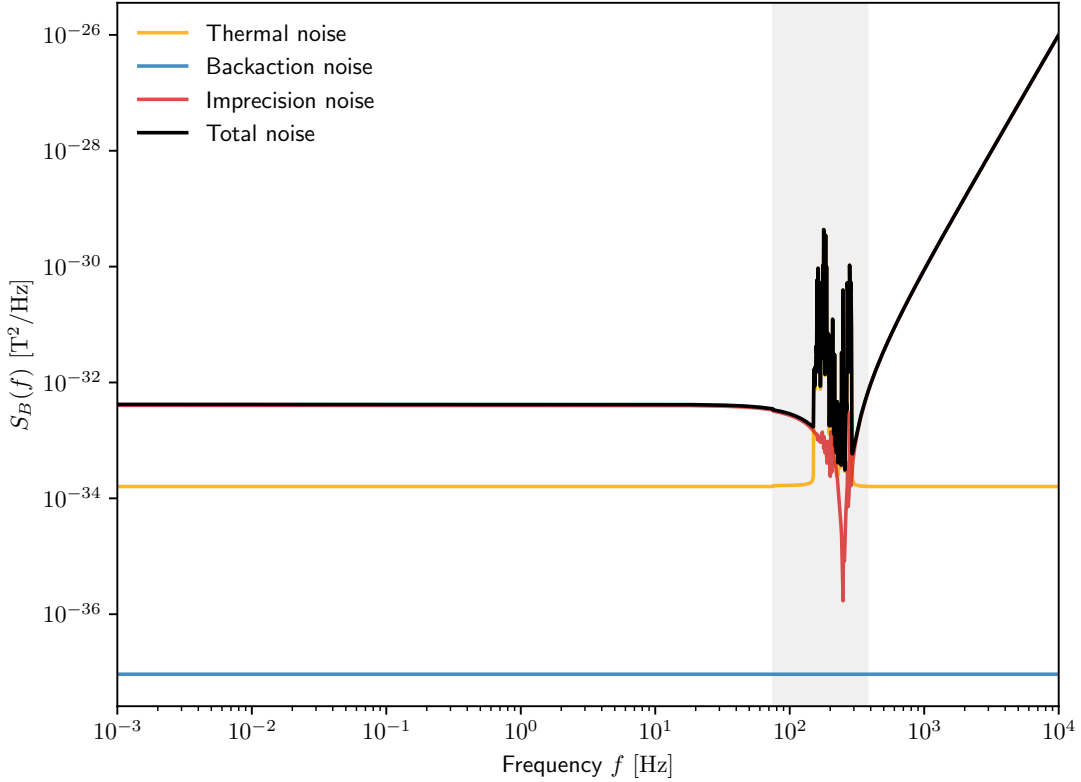


FIG. 6. Magnetic-field noise power spectral density $S_B(f)$ for the ferromagnet ensemble. The total noise (black line) is shown together with its individual contributions: thermal noise, backaction noise, and imprecision noise. The imprecision noise is evaluated using the corrected coherent susceptibility $\chi_{\text{coh}}(\omega)$, resulting in a steep rise at high frequencies. We mark the blind zone as the gray area, within which interaction severely reshapes the noise spectrum. At most frequencies, the noise is dominated by the imprecision noise, while at the blind zone the thermal noise sets the sensitivity. For the benchmark configuration, $v_{\theta\theta} = v_{\phi\phi}$, so the two bare libration frequencies coincide and only a single resonance appears.

varied independently.

Before choosing explicit numerical values, it is useful to understand the resulting scaling of the dominant noise contribution. In the sparse and macroscopic lattice configurations considered here, the leading readout limitation is typically the imprecision noise. Physically, this is because the pickup coil must enclose the full array, so the geometric coupling to each individual ferromagnet becomes weaker as the system size increases. The equivalent

magnetic-field imprecision noise scales as

$$S_B^{\text{imp}} \propto \frac{V_{\theta\theta}^2}{(N\mu\eta_{\text{eff}})^2}, \quad (126)$$

where $N\mu$ is the coherent magnetic moment of the lattice, and η_{eff} denotes the effective readout coupling after including both the geometric pickup factor and the inductive rescaling from the SQUID circuit. As discussed earlier, the coupling of the pickup coil to different momentum modes is determined only by the ratio R_p/L_{lat} , rather than by the absolute values of R_p and L_{lat} separately. One may therefore enlarge the system while preserving the readout mode profile, provided that this ratio is kept fixed. Motivated by this observation, we keep R_p/L_{lat} constant in the scaling analysis, so that changing the overall system size does not alter which lattice modes are preferentially read out. The lattice size is

$$L_{\text{lat}} \sim N^{1/3}a_0. \quad (127)$$

For a fixed coil-to-lattice aspect ratio, the effective coupling has the approximate scaling

$$\eta_{\text{eff}} \propto R^3 L_{\text{lat}}^{-\alpha}, \quad 1 \leq \alpha \leq 2, \quad (128)$$

where the two limiting cases correspond to different inductive regimes of the readout circuit. When the intermediate-coil inductance dominates over the pickup-coil inductance, $L_i \gg L_p$, one finds approximately $\alpha = 1$. When the pickup-coil inductance dominates, $L_i \ll L_p$, the coupling decreases faster with the system size, giving approximately $\alpha = 2$. More precisely, η_{eff} also contains a weak logarithmic dependence on R_p , but this only produces a mild $\ln(R_p)$ correction and does not affect the leading power-law behavior. We therefore neglect this logarithmic dependence in the following scaling estimate.

Combining Eqs. (125) and (128), together with $N \sim (L_{\text{lat}}/a_0)^3$ and $\mu \propto R^3$, gives

$$S_B^{\text{imp}} \propto L_{\text{lat}}^{2\alpha-6}. \quad (129)$$

Thus, along a family of designs with fixed λ_{int} and fixed R_p/L_{lat} , the leading imprecision-noise scaling is controlled primarily by the total lattice size. At this level, the explicit dependence on the microscopic parameters R and a_0 cancels out. In the two limiting readout regimes,

$$S_B^{\text{imp}} \propto L_{\text{lat}}^{-4} \quad (L_i \gg L_p), \quad S_B^{\text{imp}} \propto L_{\text{lat}}^{-2} \quad (L_i \ll L_p). \quad (130)$$

Therefore, within this fixed- λ_{int} scaling trajectory, enlarging the total lattice size improves the imprecision-limited sensitivity, even though the geometric coupling of an individual large pickup coil becomes weaker.

This conclusion should be distinguished from a different type of variation in which λ_{int} itself is changed. If the trapping curvature and the single-particle parameters are held fixed, increasing the lattice spacing a_0 reduces the dipole-dipole interaction strength and hence lowers λ_{int} . This is useful for suppressing interaction-induced mode mixing, but it also enlarges the physical size of a lattice with fixed N , thereby weakening the overall pickup coupling. This statement refers to the tradeoff encountered when a_0 is used to tune the interaction strength itself. It does not contradict the power law in Eq. (129), which applies after λ_{int} has already been fixed and the corresponding trapping curvature has been adjusted consistently.

The scaling analysis leads to the following parameter strategy. Since the leading imprecision-noise scaling is insensitive to the microscopic choice of R and a_0 once λ_{int} is fixed, we keep the single-ferromagnet parameters the same as those of the existing single-particle setup [10] in order to allow a direct comparison. The remaining design freedom is then used to choose a lattice spacing and trapping curvature that keep λ_{int} moderate while keeping the total lattice size within a feasible macroscopic range. For this purpose, we fix

$$\lambda_{\text{int}} = 0.0665, \quad (131)$$

and choose

$$a_0 = 100R = 2000 \text{ } \mu\text{m}. \quad (132)$$

For a lattice containing $N = 10^6$ ferromagnets, this corresponds to a $100 \times 100 \times 100$ simple-cubic lattice with total linear size

$$L_{\text{lat}} = N^{1/3}a_0 = 200 \text{ mm}. \quad (133)$$

This choice should be understood as a compromise between interaction control and experimental scale. A larger a_0 , at fixed trapping curvature, would further reduce λ_{int} , but would also enlarge the array for the same N . Conversely, a smaller a_0 would make the device more compact, but would require a larger trapping curvature in order to keep λ_{int} fixed. The benchmark value above keeps the residual interaction sufficiently weak while avoiding an excessively large lattice.

The same scaling argument also suggests a straightforward route toward further improvement: one may continue to lower the noise by increasing the total number of ferromagnets and correspondingly enlarging the lattice size. In practice, however, a larger lattice also introduces more severe technical challenges for levitation, since the trapping and stabilization of a macroscopic three-dimensional array become increasingly demanding as the system size grows.

For the chosen a_0 and target λ_{int} , we have

$$V_{\theta\theta} = V_{\phi\phi} = 10^{-13} \text{ J.} \quad (134)$$

This value keeps the angular response relatively large while maintaining the interaction strength in the perturbative regime. The equality $V_{\theta\theta} = V_{\phi\phi}$ is assumed for simplicity, so that the two transverse directions have the same bare trapping curvature.

For the collective readout, we choose the pickup-coil radius to be comparable to the lattice size,

$$R_p = L_{\text{lat}} = 200 \text{ mm.} \quad (135)$$

This implements the fixed-aspect-ratio assumption adopted in the scaling estimate above and ensures that the coil encloses the full lattice. The effective coupling to the SQUID is written as

$$\eta_{\text{eff}} = \eta \frac{M_i}{L_{\text{tot}}}, \quad (136)$$

where η is the geometric pickup coupling, M_i is the mutual inductance between the input coil and the SQUID, and L_{tot} is the total inductance of the pickup and input circuit. In the present benchmark configuration, the large lattice size makes the imprecision noise the dominant readout-induced contribution. The backaction noise cannot be raised to the same level by circuit rebalancing without simultaneously worsening the imprecision noise. Increasing the pickup-coil loop number would also increase the pickup inductance and further degrade the effective coupling in this regime. We therefore choose the minimal loop number,

$$N_p = 1. \quad (137)$$

The benchmark parameters used in the numerical calculations are summarized in Table I. Parameters marked with an asterisk are inherited directly from Ref. [10], while the lattice spacing, trapping strength, pickup-coil radius, and readout configuration are chosen here according to the scaling considerations and interaction constraints described above.

With these parameters fixed, we evaluate the magnetic-field noise spectrum of the lattice. The thermal contribution is computed using the interaction-corrected expression derived in Sec. V.B, including the boundary-induced mode mixing and the associated blind zone. The imprecision noise is obtained from the corrected coherent transfer function, while the backaction noise is determined directly by the collective pickup-circuit fluctuations. The resulting spectrum is shown in Fig. 6, where the thermal, imprecision, and backaction contributions are plotted separately together with their sum.

The resulting spectrum reflects the scaling picture discussed above. Over most of the accessible frequency range, the total noise is limited by imprecision noise, reflecting the weak effective coupling of the macroscopic pickup coil. The thermal noise remains subdominant away from the interaction-induced blind zone, where it follows the expected collective scaling. Inside the blind zone, however, boundary-mediated coupling to near-singular modes strongly amplifies the thermal contribution and sharply degrades the observable sensitivity. The backaction noise remains parametrically smaller throughout the benchmark configuration and does not set the final sensitivity floor. A SQUID detector operating with near-quantum-limited noise, or a larger lattice containing 1000 ferromagnets on each side, would be sufficient to suppress the imprecision noise below the thermal noise over a substantial part of the accessible band. In that regime, the sensitivity would no longer be set by the readout chain, but instead approach the intrinsic thermal limit of the lattice magnetometer.

VI. ULDM DETECTION

A. General signal model and SNR formalism

We now project the magnetic-field sensitivity of the ferromagnet lattice magnetometer onto several well-motivated ultralight dark matter scenarios. Each dark matter candidate considered below induces an effective oscillating magnetic-like field acting on the spins of the ferromagnets. Once this effective field is specified, the corresponding signal-to-noise ratio can be obtained directly from the noise spectrum derived in Sec. V. For all channels of interest, the dark matter field behaves as a coherently oscillating classical background on laboratory timescales. The signal can therefore be modeled as a narrowband effective

magnetic field,

$$\mathbf{B}_{\text{DM}}(t) = \mathbf{B}_0 \cos(\omega_{\text{DM}}t + \varphi), \quad (138)$$

where $\omega_{\text{DM}} \simeq m_{\text{DM}}$ is set by the dark matter mass, \mathbf{B}_0 is the channel-dependent field amplitude, and φ is an unobservable initial phase. Since the dark matter velocity distribution is nonrelativistic, the signal is not perfectly monochromatic but has a finite fractional bandwidth of order v_{DM}^2 . Equivalently, the signal possesses a finite coherence time

$$t_{\text{coh}} \sim \frac{1}{m_{\text{DM}}v_{\text{DM}}^2}, \quad (139)$$

or, in frequency space, a bandwidth

$$\delta f_{\text{DM}} \sim \frac{1}{t_{\text{coh}}}. \quad (140)$$

The magnetic-field sensitivity of the detector is described by the total noise spectral density $S_B(\omega)$ obtained in Sec. V. For a signal oscillating at frequency ω_{DM} , only the noise within the dark-matter bandwidth contributes appreciably to the measurement. The corresponding signal-to-noise ratio (SNR) may therefore be written as [10]

$$\text{SNR} = \frac{B_{\text{DM}}^2}{6} \sqrt{\text{Tr}[S_B^{-2}(\omega_{\text{DM}})] t_{\text{int}} \min(t_{\text{int}}, t_{\text{coh}})}, \quad (141)$$

where $B_{\text{DM}} = |\mathbf{B}_0|$ denotes the amplitude of the effective magnetic field, and t_{int} is the total integration time. Here the trace is taken over the two transverse response directions of the ferromagnet. The SNR improves linearly with the coherent integration time, but only up to the dark-matter coherence time. For $t_{\text{int}} \gg t_{\text{coh}}$, the measurement consists of many incoherent time segments and the net sensitivity grows only through the number of such segments. The exclusion reach for a given dark matter model is obtained by requiring that the corresponding signal remain below the detection threshold. Throughout this work we adopt the criterion

$$\text{SNR} = 3, \quad (142)$$

which defines the projected upper limit on the relevant coupling parameter at each dark matter mass. Once the channel-dependent relation between B_{DM} and the microscopic coupling is specified, the magnetic-field reach of the detector can therefore be translated directly into a projected sensitivity curve.

B. Axion-electron coupling

We first consider an axion-like particle coupled to electrons through the derivative interaction

$$\mathcal{L}_{ae} = \frac{g_{ae}}{2m_e} \partial_\mu a \bar{\psi}_e \gamma^\mu \gamma^5 \psi_e. \quad (143)$$

In the nonrelativistic limit, this interaction reduces to a coupling between the axion gradient and the electron spin, and may therefore be interpreted as an effective oscillating magnetic field acting on the ferromagnet,

$$\mathbf{B}_{ae} = \frac{g_{ae}}{\gamma_e m_e} \nabla a. \quad (144)$$

For axion dark matter, the field may be written locally as

$$a(t, \mathbf{x}) = a_{\text{DM}} \cos(\omega_{\text{DM}} t - \mathbf{k} \cdot \mathbf{x} + \varphi), \quad (145)$$

with $\omega_{\text{DM}} \simeq m_a$ and $|\mathbf{k}| = m_a v_{\text{DM}}$. Using the relation between the oscillation amplitude and the local dark matter density,

$$\rho_{\text{DM}} \simeq \frac{1}{2} m_a^2 a_{\text{DM}}^2, \quad (146)$$

one obtains

$$|\nabla a| \sim m_a v_{\text{DM}} a_{\text{DM}} = v_{\text{DM}} \sqrt{2\rho_{\text{DM}}}. \quad (147)$$

The effective magnetic field amplitude is therefore

$$B_{ae} \sim \frac{g_{ae}}{\gamma_e m_e} v_{\text{DM}} \sqrt{2\rho_{\text{DM}}}. \quad (148)$$

Several points are worth emphasizing. First, the signal amplitude in Eq. (148) is set entirely by the dark matter background and does not depend on the ferromagnet lattice itself. In this channel, the lattice does not enhance the signal-generation mechanism. Its role is instead to improve the magnetic-field sensitivity through the collective noise reduction derived in Sec. V. Accordingly, the projected improvement relative to a single ferromagnet arises solely from the reduced noise floor. Second, because the axion-wind signal is spatially uniform across the scale of the lattice, all ferromagnets experience the same effective magnetic field to an excellent approximation. The response therefore adds coherently across the array, and the noise spectrum obtained in Sec. V can be applied directly without further geometric suppression.

The projected sensitivity to the axion-electron coupling is obtained by substituting Eq. (148) into the general SNR relation, Eq. (141), and imposing the threshold condition

Eq. (142). This gives the upper limit on g_{ae} as a function of the axion mass m_a . Compared with the existing single-ferromagnet setup, the lattice improves the projected reach over the full frequency range shown by about 3 orders of magnitude, reflecting the collective reduction of the effective noise.

C. Dark photon kinetic mixing

We next consider dark-photon dark matter. In the low-energy description relevant here, the dark photon A'_μ is kinetically mixed with the ordinary photon and behaves as a coherently oscillating background vector field. Its coupling to the electromagnetic sector can be written as

$$\mathcal{L}_{A'} = -\epsilon m_{A'}^2 A'_\mu A'^\mu, \quad (149)$$

where ϵ is the kinetic-mixing parameter and $m_{A'}$ is the dark-photon mass. The dark photon field then acts as an effective source for ordinary electromagnetism,

$$J_{\text{eff}}^\mu = \epsilon m_{A'}^2 A'^\mu. \quad (150)$$

Inside a magnetically shielded apparatus, the electromagnetic response to this source is determined by the boundary conditions imposed by the shield. In the low-frequency regime relevant for the present experiment, the induced magnetic response is set parametrically by the characteristic size L_{sh} of the shielded region. Solving the induced field under these boundary conditions gives the effective magnetic-field amplitude

$$B_{A'} \sim \epsilon \sqrt{2\rho_{\text{DM}}} m_{A'} L_{\text{sh}}. \quad (151)$$

As in the axion-electron case, this signal is determined by the dark matter background together with the macroscopic shield geometry; it is not enhanced by the ferromagnet lattice itself. We stress that Eq. (151) is only an order-of-magnitude estimate of the effective magnetic field. A more precise expression would require a dedicated analysis of the electromagnetic response of the specific shield geometry.

The role of the lattice in the dark-photon channel is therefore again to reduce the detector noise rather than to modify the signal-generation mechanism. Since the induced magnetic-like field is approximately uniform across the lattice for $L_{\text{lat}} \ll L_{\text{sh}}$, all ferromagnets respond coherently and the collective readout formalism developed above remains applicable. The

projected sensitivity to the kinetic-mixing parameter ϵ is then obtained similarly as before. The lattice configuration also improves the projected dark-photon sensitivity relative to the single-ferromagnet implementation across the mass range of interest by about 4 orders of magnitude, again due to the collective improvement of the detector noise performance.

D. Axion-photon coupling

Finally, we consider the axion coupling to standard model photons,

$$\mathcal{L}_{a\gamma} = -\frac{1}{4}g_{a\gamma}aF_{\mu\nu}\tilde{F}^{\mu\nu}, \quad (152)$$

where $g_{a\gamma}$ denotes the axion-photon coupling constant. In the presence of a background electromagnetic field, the axion induces an oscillatory electromagnetic response that may be described by an effective current,

$$J_{\text{eff}}^\mu = g_{a\gamma}\partial_\nu a\tilde{F}^{\mu\nu}. \quad (153)$$

Unlike the axion-electron and dark-photon channels discussed above, the resulting signal depends explicitly on the ambient electromagnetic field and therefore on the experimental configuration itself. In the present setup, this background field is generated by the ferromagnet lattice, so that the detector does not merely probe the signal passively, but also participates directly in its generation.

Following refs. [26, 27], the axion-photon-induced magnetic field inside the shielded volume may be expanded in the cavity modes of the shield,

$$\mathbf{B}_{a\gamma}(\mathbf{r}) = \sum_n c_n \frac{f_n}{f_a} \mathbf{B}_n(\mathbf{r}) e^{-im_a t}, \quad (154)$$

with

$$c_n = -\frac{\sqrt{\hbar c^3} g_{a\gamma} f_a^2 a_{\text{DM}}}{f_n^2 - f_a^2} \int dV \mathbf{E}_n^*(\mathbf{r}) \cdot \mathbf{B}_0(\mathbf{r}), \quad (155)$$

where \mathbf{E}_n and \mathbf{B}_n are the electric and magnetic fields of the cavity modes, f_n is the mode frequency, $f_a = m_a/2\pi$, and

$$a_{\text{DM}} = \frac{\sqrt{2\rho_{\text{DM}}}}{m_a}. \quad (156)$$

The cavity modes are normalized as

$$\int dV |\mathbf{E}_n(\mathbf{r})|^2 = 1. \quad (157)$$

The signal is therefore controlled by the overlap integral

$$I_n = \int dV \mathbf{E}_n^*(\mathbf{r}) \cdot \mathbf{B}_0(\mathbf{r}). \quad (158)$$

For the shield dimensions of interest, the relevant cavity frequencies satisfy $f_n \sim c/L_{\text{sh}} \gg f_a$, so that Eq. (155) simplifies to

$$c_n \simeq -g_{a\gamma} \frac{f_a^2}{f_n^2} a_{\text{DM}} I_n. \quad (159)$$

The problem is thus reduced to estimating the scaling of I_n with the ferromagnet number N .

The background magnetic field may be decomposed as

$$\mathbf{B}_0 = \mathbf{H}_0 + \mathbf{M}, \quad (160)$$

where \mathbf{M} is the magnetization of the ferromagnets. Since there is no free current, one has $\nabla \times \mathbf{H}_0 = 0$, and hence

$$\mathbf{H}_0 = \nabla \Psi_0 \quad (161)$$

for a magnetic scalar potential Ψ_0 . The overlap integral then separates into two pieces,

$$I_n = \int dV \mathbf{E}_n^* \cdot \nabla \Psi_0 + \int dV \mathbf{E}_n^* \cdot \mathbf{M}. \quad (162)$$

Using integration by parts and $\nabla \cdot \mathbf{E}_n = 0$ inside the cavity volume, the first term reduces to a surface contribution,

$$I_n = \int d\mathbf{S} \cdot \mathbf{E}_n^* \Psi_0 + \int dV \mathbf{E}_n^* \cdot \mathbf{M}. \quad (163)$$

We first consider the surface term. The scalar potential is generated by the array of magnetic dipoles and modified by the shield. Since both the shield size and the minimum distance from the ferromagnets to the shield are much larger than the size of each individual ferromagnet, the shield-induced correction to the scalar potential is subleading for the scaling argument, and one may approximate

$$\Psi_0(\mathbf{r}) = \sum_i \frac{\boldsymbol{\mu} \cdot (\mathbf{r} - \mathbf{r}_i)}{4\pi |\mathbf{r} - \mathbf{r}_i|^3}, \quad (164)$$

where \mathbf{r}_i denotes the position of the i th ferromagnet and all dipoles are assumed aligned with the same magnetic moment $\boldsymbol{\mu}$. On the shield surface, where $|\mathbf{r}| \sim L_{\text{sh}} \gg |\mathbf{r}_i|$, this may be expanded about the geometric center of the array. Choosing the origin such that

$$\sum_i \mathbf{r}_i = 0, \quad (165)$$

the dipole expansion gives

$$\Psi_0(\mathbf{r})|_{\text{shield}} = \frac{N \boldsymbol{\mu} \cdot \mathbf{r}}{4\pi |\mathbf{r}|^3} \left[1 + \mathcal{O}\left(\frac{L_{\text{lat}}^2}{L_{\text{sh}}^2}\right) \right]. \quad (166)$$

Thus, to leading order, the surface contribution is identical to that of a single dipole carrying the effective magnetic moment

$$\boldsymbol{\mu}_{\text{eff}} = \sum_i \boldsymbol{\mu}_i = N \boldsymbol{\mu}. \quad (167)$$

We next consider the magnetization term in Eq. (163). Since each ferromagnet is much smaller than the shield and the relevant low-frequency cavity modes vary only on the scale of L , the electric field of a given cavity mode is approximately constant across each individual ferromagnet. The volume integral may therefore be approximated as

$$\int dV \mathbf{E}_n^*(\mathbf{r}) \cdot \mathbf{M} \approx \boldsymbol{\mu} \cdot \sum_i \mathbf{E}_n^*(\mathbf{r}_i). \quad (168)$$

If the array is centrally symmetric and satisfies $L_{\text{lat}} \ll L_{\text{sh}}$, the cavity field may be expanded about the array center,

$$\mathbf{E}_n(\mathbf{r}_i) = \mathbf{E}_n(0) + r_i^a \partial_a \mathbf{E}_n(0) + \frac{1}{2} r_i^a r_i^b \partial_a \partial_b \mathbf{E}_n(0) + \dots. \quad (169)$$

The linear term vanishes after summing over the array because $\sum_i \mathbf{r}_i = 0$, leaving

$$\sum_i \mathbf{E}_n^*(\mathbf{r}_i) = N \mathbf{E}_n^*(0) + \mathcal{O}(N L_{\text{lat}}^2 \partial^2 \mathbf{E}_n^*(0)). \quad (170)$$

Since the cavity-mode variation scale is set by L_{sh} , one has parametrically $\partial^2 \mathbf{E}_n \sim \mathbf{E}_n / L_{\text{sh}}^2$, and therefore

$$\int dV \mathbf{E}_n^* \cdot \mathbf{M} \approx N \boldsymbol{\mu} \cdot \mathbf{E}_n^*(0) \left[1 + \mathcal{O}\left(\frac{L_{\text{lat}}^2}{L_{\text{sh}}^2}\right) \right]. \quad (171)$$

Equations (166) and (171) show that both contributions to I_n scale linearly with N as long as the array remains small compared with the spatial variation scale of the relevant cavity modes. The overlap integral therefore takes the form

$$I_n = N I_n^{(1)} \left[1 + \mathcal{O}\left(\frac{L_{\text{lat}}^2}{L_{\text{sh}}^2}\right) \right], \quad (172)$$

where $I_n^{(1)}$ is the corresponding single-ferromagnet overlap. Substituting Eq. (172) into Eq. (159) then implies that the cavity-mode coefficients scale as

$$c_n = N c_n^{(1)} \left[1 + \mathcal{O}\left(\frac{L_{\text{lat}}^2}{L_{\text{sh}}^2}\right) \right]. \quad (173)$$

The axion-induced magnetic field experienced by the lattice is therefore enhanced by the same factor,

$$B_{a\gamma} \sim N B_{a\gamma}^{(1)}, \quad (174)$$

up to an overall geometric factor of order unity that depends on the detailed array geometry and the cavity-mode structure.

Using the single-ferromagnet estimate of Refs. [10, 26], one finally obtains

$$B_{a\gamma} \sim \mathcal{O}(0.1) N g_{a\gamma} \sqrt{2\rho_{\text{DM}}} \frac{|\mu|}{L_{\text{sh}}^2}. \quad (175)$$

This is the key distinction of the axion-photon channel: the lattice does not merely reduce the detector noise, but also enhances the signal-generation mechanism itself through the coherent buildup of the background magnetic field.

The enhancement in Eq. (175) should be understood as a property of the low-frequency cavity modes that vary only on the scale of the shield size L_{sh} . For these modes, the lattice is effectively point-like, and both contributions to the overlap integral add coherently up to corrections of order $L_{\text{lat}}^2/L_{\text{sh}}^2$. The situation is different for the higher-frequency cavity modes entering the mode sum in Eq. (154), especially in the polarization term of Eq. (163). Once the spatial variation scale of a cavity mode becomes shorter than the lattice size, different ferromagnets sample different phases of the mode function, so that the sum $\sum_i \mathbf{E}_n(\mathbf{r}_i)$ is no longer coherently enhanced. In generic situations these contributions are largely canceled, and for sufficiently symmetric array and shield geometries they may even be further suppressed by symmetry. Therefore, the high-frequency part of the polarization contribution does not receive a significant lattice enhancement and should not be expected to scale linearly with N . Nevertheless, this does not alter the overall scaling estimate, because the mode expansion is dominated by the low-frequency cavity modes for which $f_n \sim c/L_{\text{sh}}$ and the array remains effectively unresolved. These are precisely the modes that give the leading contribution to the axion-induced magnetic field. The higher-frequency modes, although present formally in the sum, contribute only subdominantly to the total field and may be neglected at the level of the present order-of-magnitude estimate. As a result, the effective magnetic field relevant for the detector response is still controlled by the low-frequency sector and therefore retains the linear scaling with the ferromagnet number,

$$B_{a\gamma} \propto N. \quad (176)$$

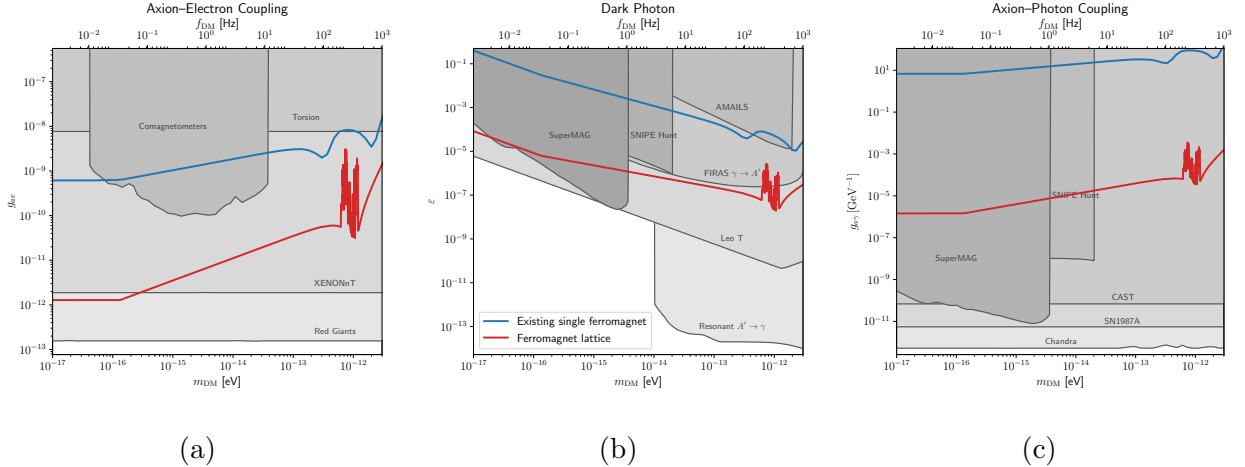


FIG. 7. The projected sensitivities derived from the ferromagnet-lattice noise spectrum are shown for axion-electron, dark-photon, and axion-photon couplings. The solid red curve shows the constraints obtained from this work. Shaded regions indicate existing constraints from the literature [28, 29]. The blue curve denotes the existing experimental constraints from a single ferromagnet magnetometer [10]. In our calculations, we take the size of the shield as $L_{\text{sh}} = 1$ m, and use the same parameter setups as the existing single ferromagnet. In all three cases, the lattice improves the reach relative to the corresponding single-ferromagnet implementation. The relative improvement is particularly pronounced in the axion-photon channel because the signal itself also receives a coherent enhancement from the lattice.

The projected sensitivity to $g_{a\gamma}$ is obtained by inserting Eq. (175) into the general SNR formula, Eq. (141), and solving for the value of $g_{a\gamma}$ that saturates the threshold condition Eq. (142) at each axion mass. In the axion-photon channel, the lattice not only benefits from the collective reduction of the effective noise, but also receives an additional signal enhancement from the coherent contribution of multiple ferromagnets to the background electromagnetic field. As a result, the improvement relative to the single-ferromagnet case is more pronounced than in the axion-electron and dark-photon channels. For the present benchmark parameters, it improves the limit by about 7 orders of magnitude.

E. Sensitivity projections

We now combine the benchmark noise spectrum obtained in Sec. V with the effective magnetic fields derived above and convert the magnetic-field reach into projected sensitivities

to the corresponding ULDM couplings. In all cases, we assume a local dark matter density ρ_{DM} , an integration time

$$t_{\text{int}} = 1 \text{ yr}, \quad (177)$$

and the detection threshold $\text{SNR} = 3$. The resulting exclusion curves are obtained by evaluating Eq. (141) at each dark matter mass and solving for the coupling value that saturates Eq. (142). The results are shown in FIG. 7.

For the axion-electron and dark-photon channels, the improvement relative to a single levitated ferromagnet originates entirely from the reduced noise floor of the lattice magnetometer. Since the effective fields in Eqs. (148) and (151) are not enhanced by the lattice itself, the projected reach tracks directly the improvement in magnetic-field sensitivity derived in Sec. V. In both cases, the gain is most significant in the low-frequency regime where the total noise is thermally limited and the collective readout suppresses the imprecision contribution most efficiently.

The axion-photon channel still benefits more strongly from increasing ferromagnet number, because the lattice lowers the noise floor and also enhances the signal itself through the collective ambient field entering Eq. (175). As a result, its improvement relative to the single-ferromagnet baseline is more pronounced than in the axion-electron and dark-photon channels. For the present benchmark parameters, however, this enhancement remains quantitative rather than qualitative and does not by itself produce a uniquely dominant reach over existing bounds.

Overall, the ferromagnet lattice improves the projected ULDM sensitivity in all three benchmark scenarios considered here. The common gain comes from collective readout and the resulting reduction of the effective noise floor. Among the three channels, the axion-photon case shows the largest relative improvement over the single-ferromagnet baseline, because the signal itself also scales favorably with the number of ferromagnets. Nevertheless, for the present benchmark setup, the main conclusion is a broad and systematic improvement across all channels rather than a uniquely dominant advantage in the axion-photon case. For further improvements, the projections shown here are based on the current SQUID noise benchmark. If the SQUID performance could be improved to the quantum limit, the projected sensitivities in all three channels would be further enhanced by approximately two orders of magnitude. With this improvement taken into account, the upper limit for the axion-electron and dark photon channel can surpass the existing bounds in a certain

frequency band.

VII. CONCLUSION

In this work, we investigated a ferromagnet lattice as a platform for ULDM detection. By replacing a single levitated ferromagnet with a coherently read-out array, the detector achieves improved sensitivity without significantly modifying the intrinsic single-particle dynamics. The central idea is to exploit collective response and readout to enhance the effective signal-to-noise ratio while retaining a well-controlled microscopic description.

We developed a theoretical framework that separates the problem into three layers. At the single-particle level, the rotational dynamics are described by a well-defined susceptibility in the fully trapped regime. At the lattice level, dipole-dipole interactions modify this response through a momentum-dependent kernel, while finite-size effects introduce boundary-induced mode mixing. These effects can be systematically incorporated as a self-energy correction to the coherent ($k = 0$) channel. This formulation makes it possible to identify the conditions under which the collective mode dominates, as well as the regimes where near-singular modes lead to strong deviations and define the blind-zone structure of the detector response.

On top of this dynamical framework, we analyzed the noise properties of the lattice detector. Thermal, imprecision, and backaction noise scale differently with the number of ferromagnets, and their interplay determines the final sensitivity. Collective readout reduces the effective noise floor, while interaction-induced mode mixing leads to a frequency-dependent modification of the thermal noise spectrum. Away from the blind-zone regime, the detector performance is well captured by an effective coherent-channel description, which provides a transparent connection between microscopic dynamics and macroscopic sensitivity.

Using this framework, we derived projected sensitivities for axion-electron, dark-photon, and axion-photon couplings. In all three channels, the lattice configuration improves the reach relative to the single-ferromagnet implementation, reflecting the collective reduction of the effective noise. In the axion-photon channel, the signal also benefits from coherent enhancement associated with the lattice-induced electromagnetic background, leading to a more pronounced improvement with increasing ferromagnet number.

The projections presented here are based on current SQUID noise benchmarks. If the SQUID performance can be improved to the quantum limit, the noise spectrum would be

further reduced by 3 orders of magnitude, corresponding to an additional improvement of approximately two orders of magnitude in the ULDM limit. Under such conditions, the axion-electron and dark-photon channels would extend beyond existing bounds over a broad frequency range.

Several directions for further improvement are suggested by the present analysis. First, the simple pickup-coil geometry considered here leads to a coupling that decreases with increasing lattice size, which becomes a limiting factor for large arrays. Optimized coil designs, or alternative readout schemes that are less sensitive to the spatial extent of the lattice, could significantly enhance the effective coupling and enable further scaling of the system size. Second, compared with the single-particle case, the lattice configuration requires the trapping potential to exceed the interaction scale, which limits the possibility of improving sensitivity by reducing the trap stiffness. If the effective interaction scale can be suppressed through dynamical control, geometric design, or other engineering approaches, the sensitivity could be substantially improved beyond the regime explored in this work.

Overall, the ferromagnet lattice provides a scalable and versatile platform for precision sensing of ultralight dark matter. The combination of collective dynamics, controllable interactions, and flexible readout architectures opens a range of opportunities for future experiments, with several plausible pathways toward further sensitivity improvements.

-
- [1] J. Preskill, M. B. Wise, and F. Wilczek, *Phys. Lett. B* **120**, 127 (1983).
 - [2] L. Abbott and P. Sikivie, *Phys. Lett. B* **120**, 133 (1983).
 - [3] M. Dine and W. Fischler, *Phys. Lett. B* **120**, 137 (1983).
 - [4] P. W. Graham, I. G. Irastorza, S. K. Lamoreaux, A. Lindner, and K. A. van Bibber, *Annu. Rev. Nucl. Part. Sci.* **65**, 485 (2015).
 - [5] P. Arias, D. Cadamuro, M. Goodsell, J. Jaeckel, J. Redondo, and A. Ringwald, *J. Cosmol. Astropart. Phys.* 06 (2012) 013–013, arXiv:1201.5902 [hep-ph].
 - [6] Y. V. Stadnik and V. V. Flambaum, *Phys. Rev. Lett.* **114**, 161301 (2015), arXiv:1412.7801 [hep-ph].
 - [7] D. Budker, P. W. Graham, M. Ledbetter, S. Rajendran, and A. O. Sushkov, *Phys. Rev. X* **4**, 021030 (2014).

- [8] P. W. Graham, J. M. Hogan, M. A. Kasevich, and S. Rajendran, *Phys. Rev. Lett.* **110**, 171102 (2013), arXiv:1206.0818 [quant-ph].
- [9] D. F. Jackson Kimball and K. Van Bibber, eds., *The Search for Ultralight Bosonic Dark Matter* (Springer International Publishing, Cham, 2023).
- [10] S. Kalia, D. Budker, D. F. J. Kimball, W. Ji, Z. Liu, A. O. Sushkov, C. Timberlake, H. Ulbricht, A. Vinante, and T. Wang, *Phys. Rev. D* **110**, 115029 (2024).
- [11] D. Yang, X. Yang, C. Sun, and J. Zhang, *Ultralight Dark Matter Detection with a Ferromagnet Lattice* (2026), arXiv:2602.17291 [hep-ph].
- [12] X. Chen, K. H. Lam, R. Chen, Z. Chen, X. Qian, J. Zhang, P. Yu, and Q. Zhou, *Appl. Phys. Lett.* **114**, 054103 (2019).
- [13] D. Foresti, M. Nabavi, M. Klingauf, A. Ferrari, and D. Poulikakos, *Proc. Natl. Acad. Sci. USA* **110**, 12549 (2013).
- [14] A. Marzo, S. A. Seah, B. W. Drinkwater, D. R. Sahoo, B. Long, and S. Subramanian, *Nat. Commun.* **6**, 8661 (2015).
- [15] D. Ya. Sukhanov and F. S. Emelyanov, *Russ. Phys. J.* **63**, 258 (2020).
- [16] Y.-H. Tseng, *PRX Quantum* **6**, 10.1103/j76m-gcpl (2025).
- [17] J. Millen, T. S. Monteiro, R. Pettit, and A. N. Vamivakas, *Rep Prog Phys* **83**, 026401 (2020).
- [18] O. Romero-Isart, A. C. Pflanze, F. Blaser, R. Kaltenbaek, N. Kiesel, M. Aspelmeyer, and J. I. Cirac, *Phys. Rev. Lett.* **107**, 020405 (2011).
- [19] G. Ranjit, M. Cunningham, K. Casey, and A. A. Geraci, *Phys. Rev. A* **93**, 053801 (2016).
- [20] M. Frimmer, J. Gieseler, and L. Novotny, *Phys. Rev. Lett.* **117**, 163601 (2016).
- [21] D. E. Chang, C. A. Regal, S. B. Papp, D. J. Wilson, J. Ye, O. Painter, H. J. Kimble, and P. Zoller, *Proc. Natl. Acad. Sci.* **107**, 1005 (2010).
- [22] S. W. de Leeuw, J. W. Perram, and E. R. Smith, *Proc. R. Soc. Lond. Ser. A* **373**, 27 (1980).
- [23] B. Stamm, L. Lagardère, É. Polack, Y. Maday, and J.-P. Piquemal, *J. Chem. Phys.* **149**, 124103 (2018).
- [24] V. Ankel *et al.*, *J. Appl. Phys.* **138**, 094505 (2025).
- [25] A. A. Clerk, M. H. Devoret, S. M. Girvin, F. Marquardt, and R. J. Schoelkopf, *Rev. Mod. Phys.* **82**, 1155 (2010).
- [26] G. Higgins, S. Kalia, and Z. Liu, *Phys. Rev. D* **109**, 055024 (2024).
- [27] S. Chaudhuri, P. W. Graham, K. Irwin, J. Mardon, S. Rajendran, and Y. Zhao, *Phys. Rev.*

D **92**, 075012 (2015).

[28] A. Caputo, A. J. Millar, C. A. J. O'Hare, and E. Vitagliano, Phys. Rev. D **104**, 095029 (2021).

[29] C. O'Hare, cajohare/axionlimits: Axionlimits, <https://cajohare.github.io/AxionLimits/> (2020).